HHS Public Access

Author manuscript

J Comput Neurosci. Author manuscript; available in PMC 2018 February 01.

Published in final edited form as:

J Comput Neurosci. 2017 February ; 42(1): 11–30. doi:10.1007/s10827-016-0624-6.

Modeling the differentiation of A- and C-type baroreceptor firing patterns

Jacob Sturdy,

Department of Structural Engineering, NTNU, Richard Birkelandsvei 1A, 7491 Trondheim, Norway

Johnny T. Ottesen, and

Department of Science, System and Models, Roskilde University, Universitetsvej 1, 4000 Roskilde, Denmark

Mette S. Olufsen

Department of Mathematics, North Carolina State University, Campus Box 8205, Raleigh, NC 27695-8205

Abstract

The baroreceptor neurons serve as the primary transducers of blood pressure for the autonomic nervous system and are thus critical in enabling the body to respond effectively to changes in blood pressure. These neurons can be separated into two types (A and C) based on the myelination of their axons and their distinct firing patterns elicited in response to specific pressure stimuli. This study has developed a comprehensive model of the afferent baroreceptor discharge built on physiological knowledge of arterial wall mechanics, firing rate responses to controlled pressure stimuli, and ion channel dynamics within the baroreceptor neurons. With this model, we were able to predict firing rates observed in previously published experiments in both A- and C-type neurons. These results were obtained by adjusting model parameters determining the maximal ion-channel conductances. The observed variation in the model parameters are hypothesized to correspond to physiological differences between A- and C-type neurons. In agreement with published experimental observations, our simulations suggest that a twofold lower potassium conductance in C-type neurons is responsible for the observed sustained basal firing, whereas a tenfold higher mechanosensitive conductance is responsible for the greater firing rate observed in A-type neurons. A better understanding of the difference between the two neuron types can potentially be used to gain more insight into the underlying pathophysiology facilitating development of targeted interventions improving baroreflex function in diseased individuals, e.g. in patients with autonomic failure, a syndrome that is difficult to diagnose in terms of its pathophysiology.

Keywords

Baroreflex model; mechanosensitivity; A- and C-type afferent baroreceptors; biophysical model; computational model

Tel: +1 (919) 515 2678, Fax: +1 (919) 513 7336, msolufse@ncsu.edu.

1 Introduction

The cardiovascular system (CVS) primarily serves to transport substances including oxygen, nutrients, hormones, carbon dioxide, and waste products (Levick (2010)). The CVS maintains homeostasis via a dominance of negative feedback control, which actively restores the system state in response to perturbations, ensuring an uninterrupted transport function. Inputs encoding the state of the CVS are critical to the system regulation. The baroreceptor neurons monitor blood pressure by sensing changes in arterial wall strain that accompany arterial wall deformation in response to changes in blood pressure. These neurons are divided into two types according to their myelination and firing rate characteristics: A-type neurons are myelinated and fire at a high frequency when the stimulus reaches a certain threshold, while C-type neurons are unmyelinated and exhibit irregular firing, typically at low frequencies Brown et al. (1976). The characteristics considered in this analysis are more representative of autoactive C-type neurons, which fire tonically below threshold pressures. The study by Munch (1992) notes that between 15% and 54% of C-type neurons exhibit tonic firing, yet the origin of these two types of C-type neurons is not well known.

As depicted in Fig. 1, the baroreceptor neurons consist of mechanosensitive sensory nerve endings primarily located in the walls of the aorta and carotid sinuses. These nerve endings connect to dendrites that carry the electrical signal to the nucleus solitary tract (NTS) (Levick (2010)), which receives input from the baroreceptor neurons as well as from other cardiovascular afferents, such as chemoreceptors. The NTS integrates these inputs into a combined signal, which is relayed to the areas of the medulla responsible for generating sympathetic, and parasympathetic efferent signals. The targets for the efferent neural signals are the heart, and the small arteries and arterioles. At these targets the signals modulate heart rate, cardiac contractility, vascular resistance and compliance to maintain homeostasis (Korner (1971); Levick (2010); Thomas (2011)).

Beyond observation of differences in the baroreceptor firing rate generated by A- and C-type neurons, Fan et al. (1999) demonstrated that selective stimulation of A- or C-type neurons elicits distinct efferent responses. Both the blood pressure and the heart rate responses are most effective when both types of neurons are stimulated; however, selective stimulation reveals that combined A- and C-type stimulation produces more than twice the change in heart rate compared to A-type or C-type stimulation alone. Additionally, selectively stimulating A-type neurons produces a greater maximal change in blood pressure than stimulation of C-type neurons alone, though the frequency of stimulation required to achieve this is much higher than the frequency required to elicit a comparable change through C-type stimulation alone. Though these two results highlight some differences between A- and C-type response, it must be noted that this study also emphasizes how the two populations of neurons contribute to the reflex response across different frequencies of stimulation, with C-type neurons dominating the response to low frequency stimulation, whereas Atype neurons primarily contribute to reflex responses at higher frequencies of stimulation.

Both neuron types are stimulated via activation of mechanosensitive ion channels (MSC) by changes in the wall strain (caused by changes in blood pressure), and thus transduce changes in the blood pressure into an electrically encoded neural signal (Brown et al. (1978); Levick

(2010)). Another observation by Li et al. (2008) from electrophysiological and anatomical studies in rats showed that A-type neurons may be separated into two subtypes A- and Ah-type, and that female rats have significantly more Ah-type neurons than male rats. Further studies by Chavez et al. (2014) of these fibers have revealed that selective stimulation of myelinated neurons in female rats exhibits a lower threshold for MAP reduction compared to male rats suggesting that Ah-type baroreceptors may provide a functionally distinct afferent pathway within the baroreflex arc.

While many aspects of baroreflex regulation have been studied extensively (Benarroch (2008)), numerous factors modulating baroreflex responses are not fully understood, e.g. the role of angiotensin in modulation of baroreflex sensitivity (Palma-Rigo et al. (2012); Saigusa and Arita (2014)), and the mechanical properties facilitating coupling of the nerve endings to the arterial wall (Brown (1980)). Both of which may be of significance in understanding the role of the baroreflex in hypertension as suggested by the recent study by Pettersen et al. (2014).

This is largely due to the difficulty associated with studying baroreceptor function at the cellular level experimentally. In particular, no studies have been able to describe the electrophysiological and mechanical characteristics of nerve endings. The typical approach involves isolating and recording electrophysiological properties in neurons that are separated from their mechanosensitive endings (Kraske et al. (1998); Snitsarev et al. (2002)). The nerve endings are best described as a branching and intertwined neural network that is integrated into the adventitial layers of the arterial wall, making it virtually impossible to experimentally isolate the nerve endings without damage (Kraske et al. (1998); Krauhs (1979)).

Despite this difficulty, studies of the cell membranes in isolated baroreceptor neurons have identified a number of ion channels and have characterized their dynamics. As discussed in a recent review by Schild and Kunze (2012), numerous ion-channels have been identified in baroreceptor neurons. This study only includes a subset of these ion-channels (extracted from previous modeling studies by Schild et al. (1994) and Li et al. (2011)), as illustrated in Fig. 2. Focus was on selecting a subset of channels allowing the model to detect differences between A- and C-type neurons response to pressure stimuli. The selected channels include (listed with the mathematical notation representing their current in parentheses): a TTX-sensitive fast sodium current($I_{Na,F}$), a sodium background current ($I_{Na,B}$), a calcium background current ($I_{Ca,B}$), a sodium-potassium exchanger current ($I_{Na,K}$), a sodium-calcium exchanger ($I_{Na,Ca}$), a calcium pump ($I_{Ca,P}$) a delayed rectifier potassium current ($I_{K,dr}$), and a 4-AP (4-aminopyridine) sensitive potassium current ($I_{K,A}$ and $I_{K,D}$). Some of the channels excluded are the calcium sensitive potassium current identified by Li et al. (2011) and the TTX insensitive sodium current present in C-type neurons. The latter channel allows C-type neurons to continue firing when exposed to TTX, while A-type neurons cease firing. This channel would have allowed us to identify another difference between the two neuron types, but given that we do not have data to evaluate this difference, we omitted this channel.

Mathematical modeling provides a way to explore the interaction between the ion-channel dynamics and the arterial wall deformation. Several previous modeling studies have investigated baroreceptor dynamics using approaches ranging from simple phenomenological models predicting the firing rate as a function of blood pressure (Spickler (1968); Ottesen (1997); Mahdi et al. (2013); Ottesen and Mehlsen (2014)) to biophysical models using a Hodgkin-Huxley type approach to describe the electrical behavior of the isolated neurons (Schild et al. (1994)). Some biophysical models (Brederode et al. (1990); Schild et al. (1994)) were designed to predict the differences in firing patterns between A-type and C-type neurons; however, these studies did not examine how changes in vessel strain stimulate the stretch-sensitive channels. Alfrey (1997) accounted for mechanosensitivity, but focused on reproducing A-type firing patterns. In addition, a number of phenomenological models Coleridge et al. (1987); Seagard et al. (1990)) describe both A- and C-type firing rates as functions of blood pressure or wall-strain, but do not consider ion-channel dynamics, and thus do not address the basis of differentiation between A- and C-type neurons.

This study aims to combine previous efforts building a fairly simple biophysical model that can distinguish between A- and C-type firing. Our model has potential to help explore system level differences that may be attributed to differences in the distribution or role of A- and C-type neurons, such as gender differences found to play a role in patients with orthostatic intolerance (Santiago et al. (2000)). Orthostatic intolerance describes the inability of an individual's body to effectively regulate changes in blood pressure caused by changes in posture, typically accompanied by frequent syncope episodes. This disorder occurs in five females for every one occurrence in males (Pickering (2002)). We speculate that this may be associated with different ratio of A- vs. Ah-fibers in males and females (see Li et al. (2008); Chavez et al. (2014)).

To study the origin of the firing patterns displayed by A- and C-type neurons. We designed an anatomically and physiologically based model that can predict arterial wall deformation, mechanoreceptor stimulation, and action potential generation. This model is shown to effectively reproduce experimentally observed responses of baroreceptor neurons to various pressure stimuli for both A- and C-type neurons. We discuss what parameters characterize the two neuron types and use the model to simulate C-type neural responses to pressure step and pulse stimuli, which have not been well characterized in previously published experimental studies.

2 Methods

2.1 Summary of experimental data

Quantitative data describing the deformation of the rat aortic arch, along with A- and C-type firing characteristics in baroreceptors within the rat aorta as well as rabbit and canine carotid arteries, were used for analyzing the model developed in this study.

Data characterizing arterial wall deformation were extracted from the experiments by Feng et al. (2007). These experiments measured the deformation of surgically isolated rat aortic arches in response to a controlled pressure stimulus.

Baroreceptor firing rate characteristics illustrating the difference between A- and C-type neurons were extracted from experiments in rats, rabbits and dogs (Brown et al. (1978); Franz et al. (1971); Saum et al. (1976); Schild (1994); Seagard et al. (1990)). The experimental procedures in these studies were similar. They were all performed *in situ* in surgically isolated or excised vessels stretched to their *in vivo* length with the baroreceptor nerve attached.

To show firing rate characteristics exhibited by baroreceptor neurons (threshold, saturation, overshoot, and adaptation), the vessels were exposed to three prototypical blood pressure stimuli including a continuous ramp increase, a step change, a sinusoidal stimulus, and a pulse pressure stimulus. Data used to validate the model against each stimulus type are described below.

A ramp stimulus (see bottom of Fig. 3A.) can be achieved using a syringe pump to infuse fluid in a vessel clamped at its outlets. The continuous infusing of fluid cause the pressure to increase at a rate of 1–2 mmHg/sec. Previously published experiments using a ramp stimulus reveal two characteristic features of baroreceptor neurons: threshold and saturation. **Threshold** characterizes the pressure at which the firing rate frequency suddenly changes. Fig. 3A shows that A-type neurons start firing when the ramp stimulus reaches a given threshold, whereas autoactive C-type neurons fire at all pressures (over the ramp) but change firing rate at the threshold pressure, Seagard et al. (1990).[1] **Saturation** refers to the pressure range over which the firing rate remains constant, i.e. when a pressure increase no longer leads to an increase in firing rate. While both A- and C-type neurons exhibit saturation, A-type neurons saturate at a higher frequency but lower pressure than C-type neurons (see Fig. 3A.).

A number of studies analyzing the response to a ramp stimulus have achieved similar results (Bolter et al. (2011); Coleridge et al. (1987); Franz et al. (1971); Munch (1992); Munch and Brown (1985); Sato et al. (1998); Spickler and Kezdi (1967); Tomomatsu et al. (1983)). Two of these studies (Coleridge et al. (1987); Spickler and Kezdi (1967)) stimulated the baroreceptor neuron with a ramped pulsatile pressure: an underlying increasing mean pressure overlaid with a pulsatile pressure. These studies observed that the pulsatile stimulus shifts the firing rate response up, but does not change the qualitative features.

In this study, we model the ramp stimulus using the linear function

$$p(t)=at+b, \quad (1)$$

where a denotes the rate of the blood pressure increase, and b the baseline pressure.

A step pressure stimulus is commonly used to characterize the dynamic response of the baroreceptor neurons, and refers to stimulation by blood pressure changed in a rapid step (up to 200 mmHg over about 100 msec) from one value to another (see Fig. 3B). Brown et al.

[1]Seagard et al. refer to A-type as Type I, and C-type as Type II.

(1978) investigated the rat aortic baroreceptor firing rate in response to four pressure steps increasing pressure from a baseline of 115 mmHg with steps of 13 (to 128), 19 (to 134), 22 (to 137), and 28 (to 143) mmHg (Fig. 3B). The characteristic response of both A- and C-type neurons to a step stimulus is an **overshoot followed by adaptation**. At the onset of the pressure increase, neurons dramatically increase their firing rate, after which it decays toward a new steady firing rate corresponding to the new pressure (see Fig. 3). Kunze and Andresen (1991) report that C-type neurons (not shown) exhibit more irregular firing patterns than A-type neurons. Yet Brown et al. (1976) report that some C-type neurons respond with an overshoot followed by rapid adaption and then sustained cessation as the step up in pressure is maintained. For both neuron types, the experiments were done over a period of 12 sec, allowing the firing rate to adapt to a new steady level of discharge. Similar responses, mostly in A-type neurons, have been observed in multiple studies (Saum et al. (1976); Vliet and West (1987)).

We model the pressure step change using the function

$$p(t)=\begin{cases} p_b & \text{if } t<t_{\text{step}} \\ p_b+\Delta p & \text{otherwise,} \end{cases} \quad (2)$$

where p_b denotes the baseline pressure and Δp the step change.

A sinusoidal pressure stimulus is typically used to analyze the firing rate dynamics in a setting mimicking *in vivo* conditions. In response, both A- and C-type baroreceptors fire sinusoidally with some phase shift (Brown et al. (1978)), though C-type baroreceptors have characteristically lower firing rates (see Fig. 3C). Spickler and Kedzi also studied the response of (presumed A-type) baroreceptors and attempted to characterize their frequency response characteristics, finding an increased activity corresponding to increased stimulus frequency (Spickler and Kezdi (1967)). Franz et al. (1971) studied the response of (presumed A-type) baroreceptors in rabbits and attempted to develop a black box input/output model of these based on signal characteristics. Their sinusoidal stimulus recordings showed similar results to those of Brown et al. (1978).

The sinusoidal stimulus is modeled as

$$p(t)=p_b+p_A\sin\left(2\pi(\omega t+\phi)\right), \quad (3)$$

where p_b denotes the baseline pressure, p_A the amplitude, and ω the stimulus frequency, and ϕ specifies the phase shift relative to a single period of the signal.

A pulse pressure stimulus refers to a step pressure increase followed by a step decrease back to the original pressure level (Fig. 3D). Saum et al. (1976) used this stimulus to investigate the response known as **Post Excitatory Depression** (PED) observed in A-type neurons. PED is a cessation of baroreceptor firing for a period of up to 10 seconds following the

sudden decrease in pressure. The cessation of firing following decreasing pressure has been observed in numerous studies beginning with the one by Bronk and Stella (1932) who noted that baroreceptor neurons cease to fire during diastole. This phenomenon was analyzed in numerous previous studies: Landgren (1952) observed effects of amplitude and duration of the pressure step on the duration of PED. Wang et al. (1991) observed that the PED duration depends on the duration and the height of the pressure step. Finally, Saum et al. (1976) demonstrated that PED may be inhibited through processes within the baroreceptor nerve fiber itself. He suggested that an electrogenic sodium pump contributes to the phenomenon. To our knowledge no studies have investigated the response of isolated C-type neurons to a pulse pressure stimulus. The pressure pulse stimulus is modeled using the function

$$p(t)=\begin{cases} p_b & \text{if } t<t_{\text{up}} \text{ or } t_{\text{down}}<t \\ p_b+\Delta p & \text{otherwise,} \end{cases} \quad (4)$$

where p_b denotes the baseline pressure and Δp the step change.

2.2 Modeling

As shown in Fig. 1, the baroreflex model consists of three components predicting arterial wall deformation, neural deformation and mechanoreceptor stimulation, and action potential generation from which firing rate is extracted. A nonlinear function relating pressure to arterial wall strain is used to predict the increased stiffening observed with an increased pressure stimulus. This model is based on experimental studies in rats (in aortic baroreceptor neurons) (Feng et al. (2007); Bezie et al. (1998)) and in sheep (in a range of large arteries) (Valdez-Jasso et al. (2009a, 2011)). Changes in wall strain drives the baroreceptor nerve ending deformation. To our knowledge no experimental studies have characterized the coupling of the nerve ending deformation to the wall strain, thus no explicit model validation can be made for this model component. For this part of the model, we incorporated ideas put forward by Alfrey (1997), Bugenhagen et al. (2010) and Mahdi et al. (2013) using the assumption that the nerve ending deformation exhibits qualitative dynamics that are similar to that associated with the baroreceptor firing rate response to a step pressure stimulus. For this study we adopt a linear viscoelastic model with two relaxation time scales of approximately 1 and 3 seconds to predict the nerve ending deformation induced by the arterial wall strain. Nerve ending deformation stimulates mechanosensitive ion channels, whose probability of opening is modeled by a sigmoidal function of the nerve ending strain. Finally, the afferent baroreceptor firing rate is calculated from the action potentials generated by a Hodgkin-Huxley type model incorporating the major ion channels identified in patch clamp studies of baroreceptor cell bodies (Schild et al. (1994)).

2.2.1 Arterial wall deformation—The large arteries, have connective tissue attaching them to the surrounding tissues and structures of the body. As a result, the vessels are pre-stretched in their longitudinal direction and therefore mainly deform axially (Fung (1996)). Several recent studies in large mammals, e.g. the sheep study by Valdez Jasso et al. (2011), have shown that arterial deformation displays nonlinear elastic and viscoelastic properties,

yet it is not clear if viscoelasticity plays a major role in arterial wall deformation within small animals (Brown et al. (1978); Boutouyrie et al. (1997)). Due to the focus of this study on data from Brown et al. (1976, 1978) and Feng et al. (2007) in rats, and Seagard et al. (1990) in dogs, we have chosen to describe wall deformation using the elastic nonlinear sigmoidal function proposed by Valdez-Jasso et al. (2011). This model accounts for the high stiffness of the arteries at both high and low pressures following

$$A(p)=(A_m-A_0)\frac{p^{\kappa_w}}{\alpha_w^{\kappa_w}+p^{\kappa_w}}+A_0, \quad (5)$$

where A_0 and A_m are the unstressed and maximum cross-sectional area, α_w represents the pressure at which $A(p) = A_m/2$, and κ_w determines the steepness of the response.

Following Fung (1993), the axisymmetric strain can be defined as

$$\varepsilon_w=\frac{r-r_0}{r},$$

where r and r_0 denote the actual and unstressed vessel radii.

Substituting $r=\sqrt{A/\pi}$ into (5) gives

$$\varepsilon_w=1-\sqrt{\frac{(\alpha_w^{\kappa_w}+p^{\kappa_w})}{\alpha_w^{\kappa_w}+R_A p^{\kappa_w}}}, \quad (6)$$

where $R_A = A_m/A_0$.

2.2.2 Nerve ending deformation and mechanoreceptor stimulation—The aortic and carotid baroreceptor nerve endings form a complex branching network within the outermost layer (the adventitia) of the arterial wall. Exiting the adventitia individual axons merge into the afferent vagal nerve (cranial nerve X) (Andresen and Kunze (1994)). Krauhs (1979) studied the anatomy of the baroreceptor-endings in the arterial walls of rat aortic arches. The nerve endings typically lay in the collagenous tissue between elastic laminae within the adventitia. They found nerve endings both with and without connective fibers attaching them to the tissues of the arterial wall. It is well known that collagenous tissues display both elastic and viscoelastic deformation (Fung (1993)); however, how these properties determine the transfer of arterial wall strain and stress to the nerve endings have, to our knowledge, neither been measured nor modeled.

In this study we model the deformation following ideas by Alfrey (1997), Bugenhagen et al. (2010), and Mahdi et al. (2013) that described the displacement of the nerve endings relative

to the total wall stretch using a model with two Voigt bodies in series with a spring. These are all in parallel with the wall deformation, ε_w, as presented in Fig. 4.

Springs have the stress-strain relation $\sigma = E\varepsilon$, while the dash-pot elements follow $\sigma=\eta\frac{d\varepsilon}{dt}$. The strain across elements in parallel is equal, while the stress of elements in series are equal. Applying these relations to the first Voigt body gives the stress-strain equation $\sigma_2=E_2\varepsilon_2+\eta_2\frac{d\varepsilon_2}{dt}$, where ε_2 is the strain across the Voigt body. The second Voigt body has a total strain ($\varepsilon_1-\varepsilon_w$) giving $\sigma_1=E_1(\varepsilon_1-\varepsilon_2)+\eta_2\frac{d}{dt}(\varepsilon_1-\varepsilon_2)$. Both σ_1 and σ_2 must be equal to the stress in the final spring element $\sigma_{ne} = E_{ne}(\varepsilon_w - \varepsilon_1)$. By substituting the derived expressions in $\sigma_2 = \sigma_{ne}$ gives the following differential equation for ε_2

$$\frac{d\varepsilon_2}{dt}=-\frac{E_2}{\eta_2}\varepsilon_2+\frac{E_{ne}}{\eta_2}(\varepsilon_w-\varepsilon_1).$$

Similarly solving $\sigma_1 = \sigma_{ne}$ yields

$$\frac{d\varepsilon_1}{dt}=-\left(\frac{E_{ne}}{\eta_1}+\frac{E_{ne}}{\eta_2}+\frac{E_1}{\eta_1}\right)\varepsilon_1+\left(\frac{E_1}{\eta_1}-\frac{E_2}{\eta_2}\right)\varepsilon_2+\left(\frac{E_{ne}}{\eta_1}-\frac{E_{ne}}{\eta_2}\right)\varepsilon_w.$$

Further details explaining this model can be found in the study by Mahdi et al. (2013).

One parameter can be eliminated by re-parameterization of this system using $\beta_i = E_i/\eta_i$ and $\alpha_i = E_{ne}/\eta_i$ giving

$$\begin{aligned}\frac{d\varepsilon_1}{dt}&=-(\alpha_1+\alpha_2+\beta_1)\varepsilon_1+(\beta_1-\beta_2)\varepsilon_2+(\alpha_1+\alpha_2)\varepsilon_w\\ \frac{d\varepsilon_2}{dt}&=-\alpha_2\varepsilon_1-\beta_2\varepsilon_2+\alpha_2\varepsilon_w,\end{aligned}\quad (7)$$

where, the total strain ε_{ne} experienced by the mechanoreceptor is given by

$$\varepsilon_{ne}=\varepsilon_w-\varepsilon_1. \quad (8)$$

Mechanosensitive ion channels: Previous studies (Sharma et al. (1995); Kraske et al. (1998); Cunningham et al. (1997); Drummond et al. (1998); Snitsarev et al. (2002)) have identified a mechanosensitive current in baroreceptor cells; however, the details of its activation and voltage-current relationship have not been fully characterized. We described the current using a simple Ohmic relation with a reversal potential E_{m}, following the study by (Alfrey (1997)). The current is thus

$$I_{\mathrm{m}}=p_o(\varepsilon_{\mathrm{ne}})g_{\mathrm{m}}(V-E_{\mathrm{m}}), \quad (9)$$

where g_m represents the maximal whole cell conductance and $p_o(\varepsilon_{ne})$ the fraction of channels open for a given strain.

Following observations by (Kraske et al. 1998, Figure 2B), we assume that the fraction of open channels p_o depends sigmoidally on the nerve ending deformation, ε_{ne}. This is quantified using a Boltzmann relationship

$$p_o(\varepsilon_{ne}) = \left\{ 1 + \exp\left(\frac{\varepsilon_{\frac{1}{2}} - \varepsilon_{ne}}{S_{\frac{1}{2}}} \right) \right\}^{-1}, \quad (10)$$

where $S_{½}$ determines the steepness of the transition, and $\varepsilon_{½}$ corresponds to the strain associated with 50% of the channels in the open state. This basic approximation assumes instantaneous dynamics, which is reasonable since the dynamics of this current is thought to be fast compared to the duration of the action potential (Kraske et al. (1998)).

2.2.3 Afferent action potential generation model—The spiking activity of the nerve ending is modeled using a simplified conductance based approach predicting action potential generation using voltage-gated channel dynamics. This model uses a single compartment to represent the spike initiation zone and assumes that the generated spikes are carried by the nerve fibers without further modulation. The approach presented here follows the previous study by Schild et al. (1994), though it includes only the following ion channels (see also Fig. 2):

- Mechanosensitive current, I_m (stretch sensitive, inward).
- TTX-sensitive fast sodium current, $I_{Na,F}$ (voltage-gated, inward).
- Sodium background current, $I_{Na,B}$ (inward).
- Calcium background current, $I_{Ca,B}$ (inward).
- Sodium-potassium pump current, $I_{Na,K}$ (outward).
- Calcium pump current, $I_{Ca,P}$ (outward).
- Sodium-Calcium exchanger current, $I_{Na,Ca}$ (outward).
- Delayed rectifier current, $I_{K,dr}$ (voltage-gated, outward).
- 4-AP sensitive potassium currents, $I_{K,A}+I_{K,D}$ (consists of two independent voltage-gated currents, outward).

These channels are chosen due to their relatively large maximal conductances as well as their importance in producing the known qualitative dynamics associated with baroreceptor firing. A Hodgkin-Huxley type neuron model is used to describe the voltage of the nerve ending (Koch and Segev (1998); Izhikevich (2007)) formulated using an equiv alent circuit with a capacitor in series with conductance pathways representing specific ways current can

flow through the membrane of the nerve fiber. The transmembrane voltage-potential V is modeled as

$$\frac{dV}{dt}=-\sum_i I_i/C_m,$$

where I_i corresponds to the total current through a particular ion channel (including the mechanosensitive channel), and C_m denotes the membrane capacitance. An equivalent circuit representation of the model is shown in Fig. 2.

For each channel, the current through the channel is given by

$$I_i=g_i a^k b^l (V-E_i), \quad (11)$$

where g_i denotes the maximum whole- in the absence of inactivation, V is the membrane potential, E_i is the reversal potential, while a and b denote the activation and inactivation gating variables, where k and l are constants. Each of the gating variables can attain a value between 1 (fully permeable to ions) and 0 (fully non-permeable). The product of these variables denotes the percentage of conducting channels. The integer power, k or l, denotes the number of gating particles which must transition in order for the channel to open or close. Assuming the particles are independent, the probability that k activating and l inactivating particles exist in the permeable state is $a^k b^l$.

The dynamics of the ion channel are determined by the gating variables, a and b, and are modeled by

$$\frac{dz}{dt}=\frac{z_\infty - z}{\tau_z},$$

where z represents the gating variable (a or b), z_∞ is the steady state value, and τ_z the characteristic time scale.

For most currents, z_∞ is assumed to exhibit a sigmoidal voltage-dependency

$$z_\infty=\left\{1+\exp\left(\frac{V_{\frac{1}{2}}-V}{S_{\frac{1}{2}}}\right)\right\}^{-1},$$

where $V_{½}$ corresponds to half-activation potential and $S_{½}$ is related to the reciprocal of the slope of the activation curve measured at $V = V_{½}$. The time constant τ (also voltage-dependent) follows a simple Gaussian form

$$\tau = A\exp[-B^2(V-V_{peak})^2]+C,$$

where A corresponds to the peak amplitude, B scales the function width, and V_{peak} corresponds to the membrane potential at which τ equals $A+C$.

The key state variables regulating channel opening and the parameters determining the total Ohmic current are given in Appendix 5. For a more thorough treatment of neuronal modeling, we suggest the works of Koch and Segev (1998) and Izhikevich (2007).

2.2.4 Firing rate calculation—The euqations presented so far described the voltage of the neuron as a continuous function of time; however, the data of interest is the firing rate measured from the timing of spikes in the originally recorded data Brown et al. (1976). An algorithm to automatically calculate the firing rate from the voltage trace described by the model allows efficient comparison of the model voltage trace to the firing rate data. The algorithm first identifies the timing of action potential spikes, and then calculates the instantaneous firing rate f as the reciprocal of the inter-spike interval.

To compute action potential timing, the algorithm first detects times, t_j, when the voltage rises above a threshold voltage, V_{ref}. It then iterates through the solution data points (V_i,t_i) and identifies a crossing if ($V_i - V_{\text{ref}}$)($V_{i-1} - V_{\text{ref}}$) < 0 and $V_i > V_{\text{ref}}$. If this condition is met then j is incremented starting from 0, and the crossing time t_j is calculated as

$$t_j = V_{\text{ref}} - V_{i-1}\Delta t/(V_i - V_{i-1}) + t_i - \Delta t, \quad (12)$$

where $\Delta t = t_i - t_{i-1}$. V_{ref} was set to 40 mV. The time between consecutive crossings, $T_j = t_j - t_{j-1}$, is used to calculate the frequency $f_j = 1/T_j$. To determine if the neuron has ceased firing, a threshold T_{max} is set. If T_{max} milliseconds pass between successive action potentials, the instantaneous firing rate is set to 0 Hz (We define T_{max} = 300 msec). Finally, piece-wise linear interpolation is used to obtain continuous firing rate f.

2.3 Parameter Estimation and Curve Fitting

Model parameters are estimated using a combination of hand tuning and automated estimation, minimizing the least squares cost

$$J(\theta) = \sum_i^N \{y_d(t_i) - y_m(t_i,\theta)\}^2, \quad (13)$$

where θ denotes the vector of model parameters, $y_d(t_i)$ the data measured at time t_i, and $y_m(t_i, \theta)$ the associated model values. Automated parameter estimation methods include the Levenberg-Marquardt method and the Nelder-Mead simplex algorithm. The Matlab (MATLAB (2015)) function *lsqnonlin* (implementing the Levenberg-Marquardt method)

was used to estimate parameters of the arterial wall model. To remedy the relatively low speed available in Matlab, for estimation of neuronal parameters and we used the Nelder-Mead optimization tool within the *JSIM* modeling environment (Butterworth et al. (2014)).

To compare model behavior to available experimental data and known qualitative features, the individual component models were first calibrated independently. Data for arterial wall deformation recorded by Feng et al. (2007) was used to calibrate the arterial wall deformation model. The nerve ending deformation model used parameter estimates reported in a previous study that fitted this model to step response recordings of baroreceptor firing rates (Mahdi et al. (2013)). The neuronal model was adjusted to reproduce the minimal and maximal firing rates present in data. Subsequently, adjustments were made to better fit the complete model to a particular experimental data with a given stimulus: ramp, sine, step and pulse pressure.

3 Results

3.1 Baseline model calibration

Arterial wall deformation predicted by (6) was compared to data extracted from studies in rat aortic baroreceptors by Feng et al. (2007) (shown in Fig. 5). This data displays wall deformation in the center of the aortic arch over a range of pressures from 0–200 mmHg (Feng et al. 2007, Figure 4B). Results shown in Fig. 5 were obtained using the Matlab function *lsqnonlin* to estimate parameters in (6) minimizing the least squares cost (13). Estimated parameter values are $R_A = 8.32$, $\alpha_w = 198$ and $\kappa_w = 2.65$.

Nerve ending deformation was calibrated to produce a response to step pressure changes that qualitatively mimicked the baroreceptor firing rate. We used parameters reported in the previous study by Mahdi et al. (2013). This study used a simple model to scale ε_{ne} directly to the nerve ending firing rate using an affine function of the nerve ending strain of the form

$$f_{af}(\varepsilon_{ne}) = s_1 \varepsilon_{ne} + s_2. \quad (14)$$

Reported parameters are $s_1 = 480$, $s_2 = 100$, $\alpha_1 = 5.0 \cdot 10^{-4}$, $\alpha_1 = 5.0 \cdot 10^{-4}$, $\alpha_2 = 4.0 \cdot 10^{-4}$, $\beta_1 = 5.0 \cdot 10^{-4}$, and $\beta_2 = 2.0 \cdot 10^{-3}$ (see (7) for more details).

Neural model parameters were initially set to values reported by Schild et al. (1994). Parameters for the mechanosensitive channel, $\varepsilon_{½}$ and $S_{½}$, were adjusted to obtain a sigmoidal relattionship of $p_o(\varepsilon_{\text{ne}})$ over the range of input pressures p present in the data (0–200 mmHg). $\varepsilon_{1/2}$ was set to correspond to the neuron strain achieved at middle pressure between threshold and saturation. The $S_{1/2}$ value was chosen similarly ensuring that p_o was nearly zero at the pressure threshold. Finally the value for $\bar{g}_m$ was chosen by finding the minimum conductance required to initiate continuous firing in the neuronal model. The resulting values used are presented in Table 3 in Appendix 5.

Two model simulated action potentials are depicted in Fig. 6. The figure shows voltage traces from simulations with a constant pressure stimulus for an A-type (circles) and C-type (triangles) neuron.

3.2 Pressure stimuli simulations

For each simulation, model parameters were estimated ensuring that the model qualitatively and quantitatively fits literature experimental data. Given these data sets are recorded under different experimental conditions and in different species (e.g. rats, cats, dogs), parameter values differ between simulations. To remedy this deficiency, the resulting parameters estimated for each stimulus were verified to produce qualitatively consistent behavior across stimuli types.

Ramp stimulus—To evaluate the model's ability to reproduce both A- and C-type firing rates, we stimulated the model with a ramp pressure (1) with slope $a = 2$ mmHg/sec. The nerve ending deformation parameters (α_1, α_2, β_1, and β_2), half activation strain, $\varepsilon_{1/2}$, and reciprocal slope, $S_{1/2}$, as well as the model's max conductances, g_i, were estimated using the Nelder-Mead method minimizing (13) between model firing rate and the A- or C-type data sets shown in Fig. 3. The initial pressure step parameters were $p_b = 100$ mmHg for the A-type simulation and $p_b = 0$ mmHg for the C-type simulation. Fig. 7 shows the resulting firing rates Table 1.

In addition to estimating parameters to fit the ramp stimulus, the estimated parameters were used to simulate model response to a step stimulus of the form (2) with base pressure $p_b =$ 135 mmHg, step amplitude $\Delta p = 22$ mmHg, and onset time $t_{\text{step}} = 1.1$ sec. This was done to determine the response of these optimized ramp responses to a step pressure input. The resulting firing rates are shown in Fig. 8.

Step stimulus—A step stimulus (2) with $p_b = 115$ mmHg, $\Delta p = 22$ mmHg, and $t_{\text{step}} = 1.1$ sec was used to simulate the experiments reported by Brown et al. (1978). Similarly to the ramp simulations, mechanical coupling parameters and neuronal conductances were estimated to fit the data (see Fig. 9 and Table 1). The estimated parameters were also used to simulate the model response to a ramp stimulus with a baseline pressure $p_b = 0$ mmHg/sec and a slope $a = 2$ mmHg/sec (the values used in the previous simulations). This was done to ensure the parameters estimated for the step response also reflected an appropriate ramp response (results not shown).

Pulse stimulus—To investigate the ability to characterize PED, the model was stimulated by a pressure pulse (4) with $p_b = 120$ mmHg, $\Delta p = 36$ mmHg, $t_{\text{up}} = 4.5$ sec, and $t_{\text{down}} = 8.6$ sec. These values were chosen to match the data from Saum et al. (1976), but with pressure values shifted to match the step stimulus used in previous simulations. Parameters were estimated minimizing (13) using the Nelder-Mead algorithm in *JSIM*. The resulting response is shown in Fig. 10A. While simulations were able to predict the baseline, overshoot, and adaptation, the duration of the PED was too short. PED can be extended to match the data (see Fig. 10B), but this is at the cost of lowering the baseline firing rate. To compare the model's behavior to that recorded by Landgren (1952), we simulated PED with pressure step

durations 2.1, 4.1 and 6.1 sec, and amplitudes of 15, 20 and 50 mmHg, see Figs. 10C and D, respectively. Finally, we used the same stimulus to simulate a C-type neuron's response to a pulse pressure stimulus, the resulting firing rates are shown in Fig. 11. To our knowledge no recordings of C-type baroreceptors' firing rate response to a pulse stimulus have been made.

Sinusoidal stimulus—To fit the firing rate response to sinusoidal data for A-type neurons recorded by Franz et al. (1971), we used a stimulus with an amplitude $p_A = 12.5$ mmHg, a mean pressure $p_b = 140$ mmHg, a frequency $\omega = 2.5$ Hz, and a phase shift $\phi = -0.1$. For this simulation parameters were estimated using the Nelder-Mead algorithm in *JSIM*. This stimulus corresponds in shape and amplitude to that used to record the data but shifted in mean pressure in order to allow a common set of neuronal parameters to be used. In addition to fitting the model parameters to A-type data, we also used the estimated parameters from the C-type ramp data (see Fig. 7) to simulate the firing rate response of a C-type neuron to the same sinusoidal stimulus. The resulting firing rates and parameters are shown in Fig. 12.

4 Discussion

The objective of this study was to develop a biophysical model of baroreceptor transduction of blood pressure that can reproduce differentiated responses of A- and C-type baroreceptor neurons. This extends existing baroreceptor models (Alfrey (1997); Bugenhagen et al. (2010); Mahdi et al. (2013)), limited by using either *ad hoc* models (Bugenhagen et al. (2010); Mahdi et al. (2013)) or by focusing on prediction of A-type dynamics (Alfrey (1997)).

The model has three components corresponding to the physical processes involved in the transduction of blood pressure: arterial wall deformation, nerve ending deformation and stimulation of mechanosensitive channels, and generation of action potentials by the neuronal membrane's ion-channel dynamics. The firing rate of the baroreceptor neurons firing rate was calculated from interspike intervals of the membrane voltage. The ion channels were characterized according to results of previous studies of baroreceptors' electrophysiological characteristics. Using this model, we were able to, both quantitatively and qualitatively, reproduce known differences between A-and C-type signaling. This was done by adjusting the parameters of the mechanical coupling (α_1, α_2, β_1, β_2, $\varepsilon_{½}$, $S_{½}$), variations of which could represent differences in the mechanosensitive propreties of different individual neurons due to variability of the anatomy of the nerve endings as well as differences between A- and C-type mechanosensitivity. Additionally, allowing E_m to vary improved the fits shown in Fig. 10 and Fig. 12, which may be interpreted as accounting for variations in the relative permeability of the mechanosensitive channel to certain ions or changes in the ionic concentrations. Changing the relative expressions of the fast sodium channel, the delayed rectifier potassium channel, the 4-AP sensitive potassium channels, the mechanosensitive channel and the sodium background current ($g_{Na,F}$, $g_{K,dr}$, $g_{K,A}$, $g_{K,D}$, g_m, and $g_{Na,B}$) also contributed to reproducing the different firing patterns in the data. The differences in these values may be attributed to individual neuron variation, differences between A- and C-type neurons, and interspecies variability. For each data set, the estimated parameter values are given in Table 1.

The parameters within the arterial wall deformation model were fit to data from Feng et al. (2007) and subsequently used in all simulations. Since, to our knowledge, no data exist showing nerve ending deformation relative to the wall deformation, the nerve ending deformation model was calibrated as suggested in a previous modeling study (Mahdi et al. (2013)), which used an integrate and fire model to predict the firing rate. We further adjusted the activation parameters, $\varepsilon_{1/2}$ and $S_{1/2}$ within the mechanosensitive ion channel and the maximal conductances, g_i, for each ion channel to reproduce available firing rate data extracted from published experiments (see Section Sect. 2.1). Other parameter values used in model of action potential generation were taken from the previous study by Schild et al. (1994).

The firing patterns for A- and C-type neurons are typically distinguished by their unique response to a ramp pressure stimulus (Seagard et al. (1990); Coleridge et al. (1987); Gilmore and Tomomatsu (1984)). A-type neurons have a distinct threshold pressure below which they do not fire, and they have a relatively large minimum firing rate (i.e. >10 Hz). C-type neurons, on the other hand, may be active over "all" pressure ranges, but have a pressure threshold at which their firing rate begins to increase in response to an increase in pressure. Their firing rage is lower than A-type neurons (between 2 and 20 Hz). These differences were reproduced in Fig. 7 by changing the relative expression of potassium currents and the strength of the mechanosensitive current. Our results agree with observations by Schild and Kunze (2012) who reported different levels of expression of potassium currents. However, no data are available quantifying differences in the mechanosensitivity between the two neuron types. Our results of fitting ramp data suggest that the C-type neurons have a lower level of current carried by the mechanosensitive pathway. This difference may be due to a difference of ion channel expression between the two neuron types, such that C-type neurons have a significantly lower density of mechanonsensitive channels in the terminal endings than the myelinated A-type neurons. Further since the C-type nerve endings are generally smaller and thus have lower surface area as reported by Krauhs (1979), the total conductance for a given channel density would also be lower. Fitting the various published experimental data by adjusting only maximal whole cell conductances and mechanical coupling parameters supports the explanation of the differences in these parameters as a reflection of neuroanatomical differences between A- and C-type terminal endings.

The difference in maximal conductance could also be attributed to differences in the channel proteins expressed in A- and C-type vagal afferent neurons and baroreceptor terminal endings (presumably mechanosensitive). The possibility of differential protein expression in A- and C-type neurons is supported by the observations of Doan et al. (2004), who found differential expression of HCN channels between A- and C-type neurons. It should be noted that no specific studies have shown that HCN channels in baroreceptor nerve endings are mechanosensitive, thus we speculate a similar difference in expression of the proteins composing the mechanosensitive channels. Doan et al. (2004) also found that blocking HCN reduced the current threshold of the nerve endings, though they were not able to prove that the observed response was independent of muscle responses to the solution used to block HCN. This finding in conjunction with the observation that C-type nerve endings have a lower HCN suggests that our observation of lower mechanosensitive conductance in C-type nerve endings may fit with the lower required current to activate nerve endings with lower

HCN expression. Further, the higher expression of an HCN current with a faster time course in Atype nerve fibers may be a part of the explanation of how A-type nerve fibers achieve much higher firing rates than C-type nerve fibers.

To our knowledge, the only reported difference between A- and C-type baroreceptors in the response to a step stimulus are that A-type neurons typically have a higher firing rate of A-type, while C-type neurons display greater irregularity Brown et al. (1978). To match the dynamics displayed by A-type neurons, the ion channel conductance was increased, especially the sodium conductance (see Fig. 9). Due to a lack of data for the step response for C-type baroreceptors, we were unable to test the model's ability to reproduce C-type data. However, we simulated a C-type response to step pressure stimulus using parameters estimated for the C-type ramp (see Fig. 8). The response obtained agrees with the qualitative features of overshoot and adaptation reported by Brown et al. (1978).

To better understand the differences associated with the individual model components, we considered how changes in individual model parameters effected the model output and found that increases in potassium conductances ($g_{K,dr}$, $g_{K,A}$, and $g_{K,D}$) generally decreased the basal firing rate, with a smaller effect on maximal firing rates. These currents may be a key determinant of the threshold pressure and necessary for converting a constantly firing C-type neuron to one that fires only above a certain pressure stimulus. Raising g_m had the greatest effect on changing maximal firing rate, and sensitivity, though it had little effect on basal firing rate. Changing $S_{½}$ and ε_h change the slope and threshold of the static pressure firing rate response observed in response to a ramp stimulus, but do not have an effect on its baseline or saturation. Increasing the half activation strain, $\varepsilon_{½}$ had a significant effect on the amount of adaptation observed in response to a pressure step stimulus. The parameters of the mechanical coupling have some effect on the baseline firing rate, though their primary effects are in the relation to the shape of the adaption curve in a step response. Increases in β_1 or β_2 result in a higher basal firing rate and a decreased scale of adaptation. Increases of α_1 or α_2 on the other hand have opposite effects.

These differences suggest that in C-type neurons the lower potassium conductance allows for sustained basal firing, whereas the higher mechanosensitive conductance is primarily responsible for the greater firing rate observed in A-type neurons. The ten fold difference between A-type and C-type g_m could be attributed to the smaller size of C-type axons and nerve endings, thus likely having a lower maximal conductance. The mechanical parameters of the C-type neuron on the other hand correspond to a greater scale of adaptation, which is particularly evident in Fig. 11. The interactions of these parameters are also important. A large change in the potassium conductance within C-type neurons can make them stop firing, and a large increase in g_m results in cessation of firing above a certain level of stimulation.

Next, we tested the models' ability to predict and modulate PED in response to changes in the duration and amplitude of the step response Fig. 10, features that, to our knowledge, has not been discussed in previous modeling studies. While the model was able to elicit PED we were not able to match all features reported in the experiment. In particular we were not able to match the duration of the PED for the given baseline and pressure step amplitude. The

model could predict a longer PED but at the cost of lowering the baseline firing rate (see Fig. 10B). As suggested by Landgren (1952) we also tested the model's ability to predict a longer PED in response to a longer or higher step. While the predicted PED was longer, results were insignificant as shown in Figs. 10C and D. This could be due to our deterministic approach to simulating neural firing or to computations in a single neuron. It is well known that introducing small amounts of noise in neural models and to include interactions among neurons can change the dynamic behavior (McDonnell and Ward (2011); Solanka et al. (2015)). However, it could also be due to misspecification of the model predicting deformation of the neuron ending, or a result of excluded channels.

Finally, we increased fast sodium conductance and decreased the background sodium current to reproduce the sinusoidal firing rate response data by Franz et al. (1971). We simulated the C-type response to sinusoidal pressure was simulated using the parameters estimated for the ramp fit. Results of this modulation were in qualitative agreement with features reported by Brown et al. (1978).

These quantitative and qualitative results indicate that a biophysical approach may indeed account for observed differences between A- and C-type neurons, primarily at the neuronal level due to electrophysiological differences. To our knowledge this is the first study that has reproduced both A- and C-type afferent firing dynamics with a single model. The predictions of the C-type response to step and pulse stimuli suggested that C-type fibers may not exhibit PED, a possibility that to our knowledge has not been discussed in previous studies. Furthermore, we predicted the C-type response to step and pulse stimuli, which provide an explanation for the characteristics of these responses, as well as suggesting that C-type fibers do not exhibit PED, a characteristic which has not been discussed in previous studies.

In addition to these differences, the model successfully reproduces the step response characteristics of the firing rate response of baroreceptors. These results are expected as we have developed a model that attempts to incorporate the characteristics of the underlying systems generating the firing rate response: the arterial wall mechanics and action potential generation in the afferent fiber endings. We observe that the variations in α_1, α_2, β_1, and β_2 seem to be greater within the group of A- type estimates as compared to those between A- and C-type ramp estimates (see Table 1), thus we hypothesize that the mechanical coupling of the fiber endings is not significantly differentiated between A- and C-type nerve endings. In fact these variations are quite large (2–3 fold) within the same nerve ending type. We hypothesize that this variability may be due to the convoluted and variable anatomical structure of the nerve endings as reported by Krauhs (1979). In addition, this variability could suggest that a single set of coupling parameters may not accurately describe the coupling of sensory endings in general.

The data available span a large range of firing rate responses indicating significant variability within individual baroreceptor types. Our results show that modeling can provide a way to investigate differences between baroreceptor types, although limited to considering autoactive C-type fibers. Although this model of autoactive C-type fibers may not explain the irregular firing observed in non-autoactive C-type fibers, it may be useful to to explain

differences between A- and Ah- type neurons studied by Li et al. (2008). The latter is of particular importance as this neuron-type may be essential to better understand pathophysiology associated in patients experiencing orthostatic intolerance.

One difficulty in this study is the lack of a data set containing recordings from a single nerve fiber's firing patterns in response to each of the stimuli considered in this study. Such a recording would ideally allow for a more consistent set of parameters to be used when reproducing each of the known firing patterns. The majority of firing rate recordings in response to a controlled pressure stimulus seem to have been conducted on A-type nerve fibers, making it difficult to evaluate the model's ability to capture the key features of C-type firing patterns. In addition, the lack of measurements of the coupling of the mechanosensitive currents to arterial wall deformation impedes better calibration and evaluation of the model's representation of these components.

Finally, our study included only the largest inward and outward currents reported in previous electrophysiology and modeling studies in order to simplify the analysis. Other ion channels may play a significant role in long-term adaptation and pharmacological sensitivities of the baroreceptor firing patterns. For example, Gallego and Eyzaguirre (1978) demonstrated that the Nav1.8 (TTX-R) channel enabled vagal afferents to conduct and produce action potentials in the presence of TTX, although not without pronounced changes in electrical threshold and action potential shape. Likewise they showed that BK-type calcium activated potassium (KCa1.1) is markedly expressed in un-myelinated vagal afferents and has been shown to be a robust modifier of neural discharge. Further studies should investigate the impact of adding more channels to study how these impact observed dynamics. In addition, various studies have identified specific ion channels using pharmacological, immunohistochemical, and genetic techniques (Schild and Kunze 2012, Table 1). These are examples of voltage-gated and calcium-activated ion channels, which carry potassium, sodium, and calcium currents are found in baroreceptor neurons though their role in determining the firing rate is not described in detail. It is possible that some of these channels contribute to dynamic fluctuations in calcium concentrations and thus contribute to frequency adaptation characteristics observed by Brown et al. (1978).

In summary, this study demonstrates the feasibility of a biophysical approach to map the differentiation between A- and C-type baroreceptor firing patterns using a common mathematical model based on the underlying physiology of the transduction process. Further work is needed to develop a comprehensive biophysical representation of the origin of the various baroreceptor firing characteristics, allowing for quantitative attribution of emergent firing rate features to particular variations in model parameters. Such an approach would provide a biophysical context for evaluating afferent baroreflex dysfunction, as this type of model would allow investigation of how physiological abnormalities may give rise to questions in the transduction of blood pressure. This model could be used to understand how selective inhibition of A- or C-type might occur and give rise to baroreflex dysfunction, which could correspond to unique etiologies of disorders such as orthostatic intolerance.

References

Alfrey, KD. PhD thesis. Rice University; Houston, TX: 1997. A model of the aortic baroreceptor in rat.

Andresen MC, Kunze DL. Nucleus Tractus Solitarius a gateway to neural circulatory control. Ann Rev Physiol. 1994; 56:93–116. [PubMed: 7912060]

Benarroch EE. The arterial baroreflex functional organization and involvement in neurologic disease. Neurology. 2008; 71:1733–1738. [PubMed: 19015490]

Bezie Y, Lamaziere JM, Laurent S, Challande P, Cunha RS, Bonnet J, Lacolley P. Fibronectin expression and aortic wall elastic modulus in spontaneously hypertensive rats. Arterioscler Thromb Vasc Biol. 1998; 18:1027–1034. [PubMed: 9672062]

Bolter CP, Turner MJ, Barrett CJ. The relationship between aortic baroreceptor activity and arterial pressure is not monotonic. J Physiol Sci. 2011; 61:151–160. [PubMed: 21240644]

Boutouyrie P, Bézie Y, Lacolley P, Challande P, Chamiot-Clerc P, Benetos A, Faverie JFRdl, Safar M, Laurent Sa. In Vivo/In Vitro Comparison of Rat Abdominal Aorta Wall Viscosity Influence of Endothelial Function. Arteriosclerosis, Thrombosis, and Vascular Biology. 1997; 17(7):1346–1355. DOI: 10.1161/01.ATV.17.7.1346

Brederode, JFv, Seagard, JL., Dean, C., Hopp, FA., Kampine, JP. Experimental and modeling study of the excitability of carotid sinus baroreceptors. Circ Res. 1990; 66:1510–1525. [PubMed: 1971534]

Bronk DW, Stella G. Afferent impulses in the carotid sinus nerve I. The relation of the discharge from single end organs to arterial blood pressure. J Cell Comp Physiol. 1932; 1:113–130.

Brown AM. Receptors under pressure. An update on baroreceptors. Circ Res. 1980; 42:694–702.

Brown AM, Saum WR, Tuley FH. A comparison of aortic baroreceptor discharge in normotensive and spontaneously hypertensive rats. Circ Res. 1976; 39:488–496. [PubMed: 183911]

Brown AM, Saum WR, Yasui S. Baroreceptor dynamics and their relationship to afferent fiber type and hypertension. Circ Res. 1978; 42:694–702. [PubMed: 639192]

Bugenhagen SM, Cowley AW, Beard DA. Identifying physiological origins of baroreflex dysfunction in salt-sensitive hypertension in the Dahl SS rat. Physiol Genomics. 2010; 42:23–41. [PubMed: 20354102]

Butterworth E, Jardine BE, Raymond GM, Neal ML, Bassingthwaighte JB. JSim, an open-source modeling system for data analysis. F1000 Res. 2014

Chavez, GCSC., Li, B-Y., Glazebrook, PA., Kunze, DL., Schild, JH. An afferent explanation for sexual dimorphism in the aortic baroreflex of rat. American Journal of Physiology - Heart and Circulatory Physiology, 00332–2014. 2014. http://ajpheart.physiology.org/content/early/2014/07/14/ajpheart.00332.2014

Coleridge HM, Coleridge JC, Schultz HD. Characteristics of C fibre baroreceptors in the carotid sinus of dogs. J Physiol. 1987; 394:291–313. [PubMed: 3443968]

Cunningham JT, Wachtel RE, Abboud FM. Mechanical stimulation of neurites generates an inward current in putative aortic baroreceptor neurons in vitro. Brain Res. 1997; 757:149–154. [PubMed: 9200510]

Doan TN, Stephans K, Ramirez AN, Glazebrook PA, Andresen MC, Kunze DL. Differential distribution and function of hyperpolarization-activated channels in sensory neurons and mechanosensitive fibers. J Neurosci. 2004; 24:3335–3343. [PubMed: 15056713]

Drummond HA, Price MP, Welsh MJ, Abboud FM. A molecular component of the arterial baroreceptor mechanotransducer. Neuron. 1998; 21:1435–1441. [PubMed: 9883735]

Fan W, Schild JH, Andresen MC. Graded and dynamic reflex summation of myelinated and unmyelinated rat aortic baroreceptors. Am J Physiol. 1999; 277:748–756.

Feng B, Li BY, Nauman EA, Schild JH. Theoretical and electrophysiological evidence for axial loading about aortic baroreceptor nerve terminals in rats. Am J Physiol. 2007; 293:3659–3672.

Franz GN, Scher AM, Ito CS. Small signal characteristics of carotid sinus baroreceptors of rabbits. J Appl Physiol. 1971; 30:527–535. [PubMed: 5572769]

Fung, YC. Biomechanics mechanical properties of living tissues. 2. Springer; New York, NY: 1993.

Fung, YC. Biomechanics circulation. Springer; New York, NY: 1996.

Gallego R, Eyzaguirre C. Membrane and action potential characteristics of a and c nodose ganglion cells studied in whole ganglia and in tissue slices. J Neurophysiol. 1978; 41:1217–1232. [PubMed: 702193]

Gilmore JP, Tomomatsu E. Comparison of carotid sinus baroreceptors in dogs, cats, monkeys, and rabbits. Am J Physiol. 1984; 247:52–56.

Izhikevich, EM. Dynamical systems in neuroscience. The geometry of excitability and bursting. MIT press; Canbridge, MA: 2007.

Koch, C., Segev, I. Methods in neuronal modeling from synapses to networks. 2. MIT Press; Cambridge, MA: 1998.

Korner PI. Integrative neural cardiovascular control. Physiol Rev. 1971; 51:312–367. [PubMed: 4930497]

Kraske S, Cunningham JT, Hajduczok G, Chapleau MW, Abboud FM, Wachtel RE. Mechanosensitive ion channels in putative aortic baroreceptor neurons. Am J Physiol. 1998; 275:1497–1501.

Krauhs JM. Structure of rat aortic baroreceptors and their relationship to connective tissue. J Neurocytol. 1979; 8:401–414. [PubMed: 490188]

Kunze, DL., Andresen, MC. Arterial baroreceptors, excitation and modulation. In: Zucker, IH., Gilmore, JP., editors. Reflex control of the circulation. CRC Press; Boca Raton, FL: 1991. p. 139-164.

Landgren W. On the excitation mechanism of the carotid baroreceptors. Acta Physiol Scand. 1952; 26:1–34. [PubMed: 12985395]

Levick, JR. An introduction to cardiovascular physiology. 5. Hodder Arnold; London, UK: 2010.

Li BY, Schild JH. Electrophysiological and pharmacological validation of vagal afferent fiber type of neurons enzymatically isolated from rat nodose ganglia. J Neurosci Methods. 2007; 164:75–85. [PubMed: 17512602]

Li BY, Qiao GF, Feng B, Zhao RB, Lu YJ, Schild JH. Electrophysiological and neuroanatomical evidence of sexual dimorphism in aortic baroreceptor and vagal afferents in rat. Am J Physiol. 2008; 295:1301–1310.

Li BY, Glazebrook P, Kunze DL, Schild JH. KCa1.1 channel contributes to cell excitability in unmyelinated but not myelinated rat vagal afferents. Am J Physiol. 2011; 300:1393–1403.

Mahdi A, Ottesen JT, Olufsen MS. Qualitative features of a novel baroreceptor model. Proc Int Workshop on Innovative Simul for Health Care. 2012:89–94.

Mahdi A, Sturdy J, Ottesen JT, Olufsen MS. Modeling the afferent dynamics of the baroreflex control system. PLoS Comput Biol. 2013; 9:1003384.

MATLAB, *version 8.5.0 (R2015a)*. The MathWorks Inc; Natick, MA: 2015.

McDonnell MD, Ward LM. The benefits of noise in neural systems: bridging theory and experiment. Nature Reviews Neuroscience. 2011; 12:415–426.

Munch PA. Discharge characteristics and rapid resetting of autoactive aortic baroreceptors in rats. J Physiol. 1992; 458:501–517. [PubMed: 1302276]

Munch PA, Brown AM. Role of vessel wall in acute resetting of aortic baroreceptors. Am J Physiol. 1985; 248:843–852.

Olufsen MS, Whittington MA, Camperi M, Kopell N. New roles for the gamma rhythm: Population tuning and preprocessing for the beta rhythm. J Comp Neurosci. 2003; 14:33–54.

Ottesen JT. Nonlinearity of baroreceptor nerves. Surv Math Ind. 1997; 7:187–201.

Ottesen JT, Mehlsen J, Olufsen MS. Structural correlation method for model reduction and practical estimation of patient specific parameters illustrated on heart rate regulation. Math Biosci. 2014:50–59.

Palma-Rigo K, Bassi JK, Nguyen-Huu TP, Jackson KL, Davern PJ, Chen D, Elghozi JL, Thomas WG, Allen AM, Head GA. Angiotensin 1a receptors transfected into caudal ventrolateral medulla inhibit baroreflex gain and stress responses. Cardiovasc Res. 2012; 96:330–339. [PubMed: 22869618]

Pettersen KH, Bugenhagen SM, Nauman J, Beard DA, Omholt SA. Arterial stiffening provides sufficient explanation for primary hypertension. PLoS Comput Biol. 2014; 10:003634.

Pickering TG. Orthostatic intolerance. J Clin Hypertens. 2002; 4:306–308.

Saigusa T, Arita J. ANG II modulates both slow and rapid baroreflex responses of barosensitive bulbospinal neurons in the rabbit rostral ventrolateral medulla. Am J Physiol. 2014; 306:538–551.

Santiago S, Ferrer T, Espinosa ML. Neurophysiological studies of thin myelinated (a delta) and unmyelinated (c) fibers: application to peripheral neuropathies. Neurophysiol Clin. 2000; 30:27–42. [PubMed: 10740794]

Sato T, Kawada T, Shishido T, Miyano H, Inagaki M, Miyashita H, Sugimachi M, Knuepfer MM, Sunagawa K. Dynamic transduction properties of in situ baroreceptors of rabbit aortic depressor nerve. Am J Physiol. 1998; 274:358–365.

Saum WR, Brown AM, Tuley FH. An electrogenic sodium pump and baroreceptor function in normotensive and spontaneously hypertensive rats. Circ Res. 1976; 39:497–505. [PubMed: 963833]

Schild JH, Kunze DL. Differential distribution of voltage-gated channels in myelinated and unmyelinated baroreceptor afferents. Auton neurosci. 2012; 172:4–12. [PubMed: 23146622]

Schild JH, Clark JW, Hay M, Mendelowitz D, Andresen MC, Kunze DL. A- and C-type rat nodose sensory neurons: model interpretations of dynamic discharge characteristics. J Neurophysiol. 1994; 71:2338–2358. [PubMed: 7523613]

Schild, JH. PhD thesis. Rice University; Houston, TX: 1994. A mathematical model of the afferent stage of the mammalian baroreceptor reflex. http://hdl.handle.net/1911/16772

Seagard JL, Brederode JFv, Dean C, Hopp FA, Gallenberg LA, Kampine JP. Firing characteristics of single-fiber carotid sinus baroreceptors. Circ Res. 1990; 66:1499–1509. [PubMed: 2344663]

Sharma RV, Chapleau MW, Hajduczok G, Wachtel RE, Waite LJ, Bhalla RC, Abboud FM. Mechanical stimulation increases intracellular calcium concentration in nodose sensory neurons. Neuroscience. 1995; 66:433–441. [PubMed: 7477884]

Snitsarev V, Whiteis CA, Abboud FM, Chapleau MW. Mechanosensory transduction of vagal and baroreceptor afferents revealed by study of isolated nodose neurons in culture. Auton Neurosci. 2002; 98:59–63. [PubMed: 12144042]

Solanka L, van Rossum MC, NMF. Noise promotes independent control of gamma oscillations and grid firing within recurrent attractor networks. Elife. 2015; 4:10–755406444.

Spickler, JW. PhD thesis. Northwestern University; Chicago, IL: 1968. Transduction properties of the carotid sinus baroreceptors.

Spickler JW, Kezdi P. Dynamic response characteristics of carotid sinus baroreceptors. Am J Physiol. 1967; 212:472–476. [PubMed: 6018034]

Thomas GD. Neural control of the circulation. Adv Physiol Edu. 2011; 35:28–32.

Tomomatsu E, Huffman L, Gilmore JP. Carotid sinus baroreceptor activity in the nonhuman primate. Circ Res. 1983; 52:380–386. [PubMed: 6831656]

Valdez-Jasso D, Haider MA, Banks HT, Santana DB, German YZ, Armentano RL, Olufsen MS. Analysis of viscoelastic wall properties in ovine arteries. IEEE Trans Biomed Eng. 2009a; 56:210–219. [PubMed: 19272946]

Valdez-Jasso D, Bia D, Zocalo Y, Armentano RL, Banks HT, Haider MA, Olufsen MS. Viscoelastic models for passive arterial wall dynamics. Adv Appl Math Mech. 2009b; 1:151–165.

Valdez-Jasso D, Bia D, Zocalo Y, Armentano RL, Haider MA, Olufsen MS. Linear and nonlinear viscoelastic modeling of aorta and carotid pressure area dynamics under in-vivo and ex-vivo conditions. Ann Biomed Eng. 2011; 39:1438–1456. [PubMed: 21203846]

Vliet BNV, West NH. Response characteristics of pulmocutaneous arterial baroreceptors in the toad, Bufo marinus. J Physiol. 1987; 388:55–70. [PubMed: 3116218]

Wang W, Chen JS, Zucker IH. Postexcitatory depression of baroreceptors in dogs with experimental heart failure. Am J Physiol. 1991; 260:1160–1165.

5 Appendix

5.1 Model equations

5.1.1 Arterial wall deformation

Nonlinear (sigmoidal) relation between vessel area A and blood pressure p:

$$A(p)=(A_m-A_0)\frac{p^k}{\alpha_w^k+p^k}+A_0.$$

Vessel strain ε_w:

$$\varepsilon_w=\frac{r-r_0}{r}=1-\sqrt{\frac{(\alpha_w^k+p^k)}{\alpha_w^k+R_A p^k}}.$$

where $R_A = A_m/A_0$.

5.1.2 Nerve ending deformation

Neuron ending deformation ε_{ne} predicted using the two-element Voigt body model in Fig. 4:

$$\frac{d\varepsilon_1}{dt}=-(\alpha_1+\alpha_2+\beta_1)\varepsilon_1+(\beta_1-\beta_2)\varepsilon_2+(\alpha_1+\alpha_2)\varepsilon_w,$$
$$\frac{d\varepsilon_2}{dt}=-\alpha_2\varepsilon_1-\beta_2\varepsilon_2+\alpha_2\varepsilon_w,$$

where

$$\varepsilon_{ne}=\varepsilon_w-\varepsilon_1.$$

5.1.3 Mechanosensitive ionic current

$$p_o(\varepsilon_{ne})=\left\{1+\exp\left(\frac{\varepsilon_{\frac{1}{2}}-\varepsilon_{ne}}{S_{\frac{1}{2}}}\right)\right\}^{-1}.$$
$$I_{\mathrm{m}}=p_o(\varepsilon_{ne})g_{\mathrm{m}}(V-E_{\mathrm{msc}}).$$

5.1.4 Conductance based model of afferent action potential generation

The reversal potentials of the ions are calculated using the Nernst equation

$$E_X=\frac{RT}{F}\ln\left(\frac{[\mathrm{X}^+]_{\mathrm{out}}}{[\mathrm{X}^+]_{\mathrm{in}}}\right).$$

The membrane voltage is governed by

$$\frac{dV}{dt} = -\sum I_i / C_m.$$

Fast sodium current:

$$\begin{aligned} I_{\mathrm{Na,F}} &= g_{\mathrm{Na,F}} m^3 h j (V - E_{Na}), \\ \frac{dm_f}{dt} &= \frac{m_\infty - m}{\tau_m}, \\ \frac{dh_f}{dt} &= \frac{h_\infty - h}{\tau_h}, \\ \frac{dj_f}{dt} &= \frac{j_\infty - j}{\tau_j}, \end{aligned}$$

and

$$\begin{aligned} m_\infty(V) &= \frac{1}{1+\exp\{-(V+41.35)/4.75\}}, \\ h_\infty(V) &= \frac{1}{1+\exp\{(V+62.00)/4.50\}}, \\ j_\infty(V) &= \frac{1}{1+\exp\{(V+40.00)/1.50\}}, \\ \tau_m(V) &= 0.75\exp\{-(0.0635)^2(V+40.35)^2\}, +0.12 \\ \tau_h(V) &= 6.50\exp\{-(0.0295)^2(V+75.00)^2\}, +0.55 \\ \tau_j(V) &= \frac{25}{1+\exp\{(V-20.00)/4.50\}} + 0.01. \end{aligned}$$

Delayed rectifier potassium current:

$$\begin{aligned} I_{\mathrm{K,dr}} &= g_{\mathrm{K,dr}} n (V - E_{\mathrm{K}}), \\ \frac{dn}{dt} &= \frac{n_\infty - n}{\tau_n}, \\ n_\infty(V) &= \frac{1}{1+\exp\{(V+14.62)/18.38\}}, \\ \tau_n(V) &= \frac{1}{\alpha_n + \beta_n} + 1.0, \\ \alpha_n &= \frac{0.001265(V+14.273)}{1-\exp\{-(V+14.273)/10\}}, \\ \beta_n &= 0.0125\exp\left(\frac{-(V+55)}{2.5}\right). \end{aligned}$$

4-AP sensitive potassium currents:

$$\begin{aligned} I_{\mathrm{K,A}} &= g_{\mathrm{K,A}} p^3 q (V - E_{\mathrm{K}}), \\ \frac{dp}{dt} &= \frac{p_\infty - p}{\tau_p}, \\ \frac{dq}{dt} &= \frac{q_\infty - q}{\tau_q}, \\ p_\infty &= \{1+\exp(-(V+28.0)/28.0)\}^{-1}, \\ q_\infty &= \{1+\exp((V+58.00)/7.0)\}^{-1}, \\ \tau_p &= 5.0\exp\{-(0.022)^2(V+65.0)^2\} + 2.5, \\ \tau_q &= 100.0\exp\{-(0.035)^2(V+30.00)^2\}, +10.5, \end{aligned}$$

and

$$
\begin{aligned}
I_{\mathrm{K,D}} &= g_{\mathrm{K,D}} x^3 y (V - E_{\mathrm{K}}), \\
\frac{dx}{dt} &= \frac{x_\infty - x}{\tau_x}, \\
\frac{dy}{dt} &= \frac{y_\infty - y}{\tau_y}, \\
x_\infty &= \{1 + \exp(-(V + 39.59)/14.68)\}^{-1}, \\
y_\infty &= \{1 + \exp((V + 48.00)/7.0)\}^{-1}, \\
\tau_x &= 5.0 \exp(-(0.022)^2 (V + 65.0)^2) + 2.5, \\
\tau_y &= 7500.0.
\end{aligned}
$$

Leakage currents:

$$
\begin{aligned}
I_{\mathrm{Na,B}} &= g_{\mathrm{Na,B}} (V - E_{Na}). \\
I_{\mathrm{Ca,B}} &= g_{\mathrm{Ca,B}} (V - E_{Ca}).
\end{aligned}
$$

Sodium-potassium exchange current:

$$
I_{\mathrm{Na,K}} = \overline{I}_{NaK} \left(\frac{[\mathrm{Na}^+]_i}{[\mathrm{Na}^+]_i + K_{M,Na}} \right)^3 \left(\frac{[\mathrm{K}^+]_o}{[\mathrm{K}^+]_o + K_{M,K}} \right)^2.
$$

Sodium-calcium exchange current:

$$
\begin{gathered}
S = 1 + D_{NaCa} \left([\mathrm{Ca}^+]_i [\mathrm{Na}^+]_o^3 + [\mathrm{Ca}^+]_o [\mathrm{Na}^+]_i^3 \right), \\
DF_{in} = [\mathrm{Na}^+]_o^3 [\mathrm{Ca}^+]_o \exp(\gamma V F / RT), \\
DF_{out} = [\mathrm{Na}^+]_o^3 [\mathrm{Ca}^+]_i \exp\{(\gamma - 1) V F / RT\}, \\
I_{\mathrm{Na,Ca}} = K_{\mathrm{Na,Ca}} (DF_{\mathrm{in}} - DF_{\mathrm{out}})/S.
\end{gathered}
$$

Calcium pump:

$$
I_{\mathrm{Ca,P}} = \overline{I}_{\mathrm{CaP}} \frac{[\mathrm{Ca}^+]_i}{[\mathrm{Ca}^+]_i + \overline{K}_{Ca}}.
$$

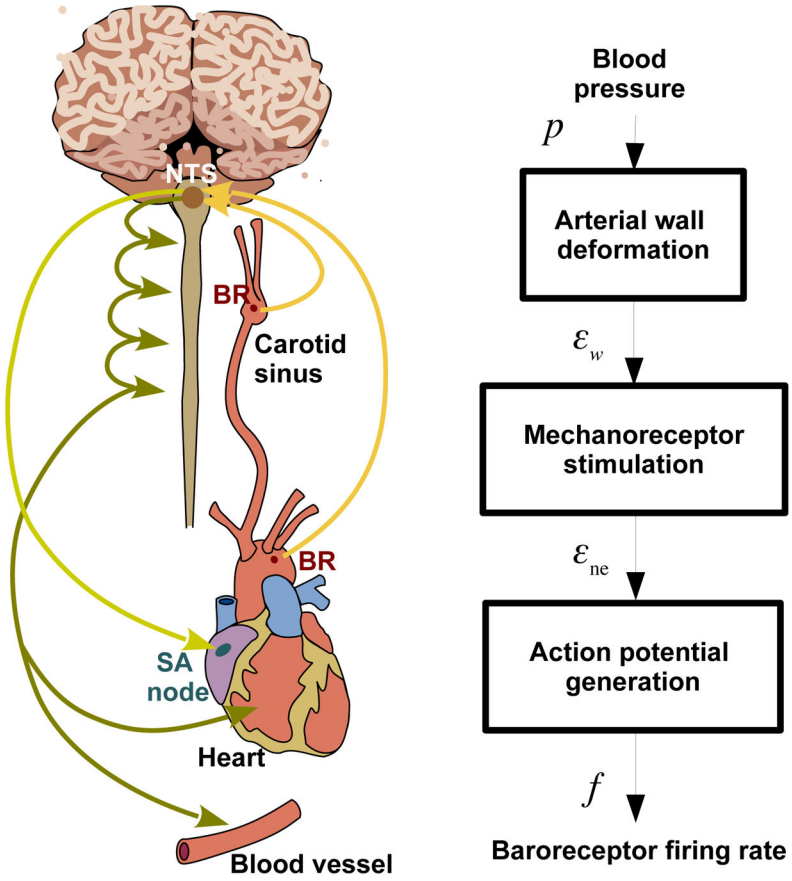

Fig. 1.

The organs and pathways associated with the baroreflex control system are shown on the left. The system's response to a drop in blood pressure includes a decrease in the aortic baoreceptor firing rate, encoding the detected change in arterial wall strain. This signal propagates along afferent baroreceptor fibers to the NTS, which integrates this information into the sympathetic and parasympathetic nervous systems. These in turn increase heart rate, cardiac contractility, and vascular resistance, and decrease vascular compliance. The right panel shows the modeling framework as a block diagram representing the biophysical basis of baroreceptor firing in response to an applied blood pressure stimulus. Abbreviations: BR (baroreceptor nerve endign), NTS (Nucleus Solitary Tract), SA (Sino Atrial node), p (arterial blood pressure), ε_w (arterial wall strain), ε_{ne} (nerve ending strain), and f (baroreceptor firing rate).

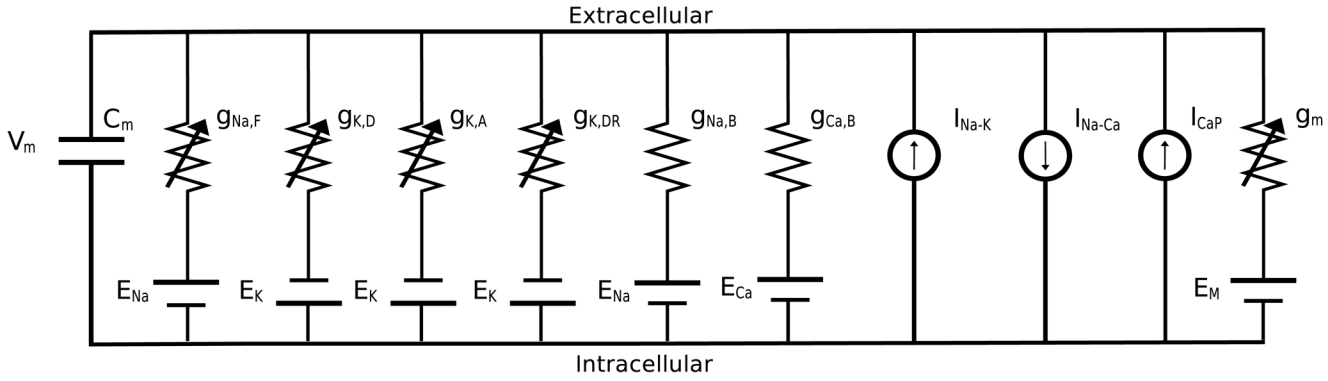

Fig. 2.

The main channels associated with afferent baroreceptor fibers are a mechanosensitive conductance (g_m), a fast sodium conductance ($g_{Na,F}$), 4-AP sensitive potassium conductances ($g_{K,A}$ and $g_{K,D}$), a delayed rectifier conductance ($g_{K,dr}$), linear leakage conductances ($g_{Na,B}$ and $g_{Ca,B}$), a sodium-potassium exchanger current ($I_{Na,K}$), a sodium-calcium exchanger ($I_{Na,Ca}$), and a calcium pump ($I_{Ca,P}$).

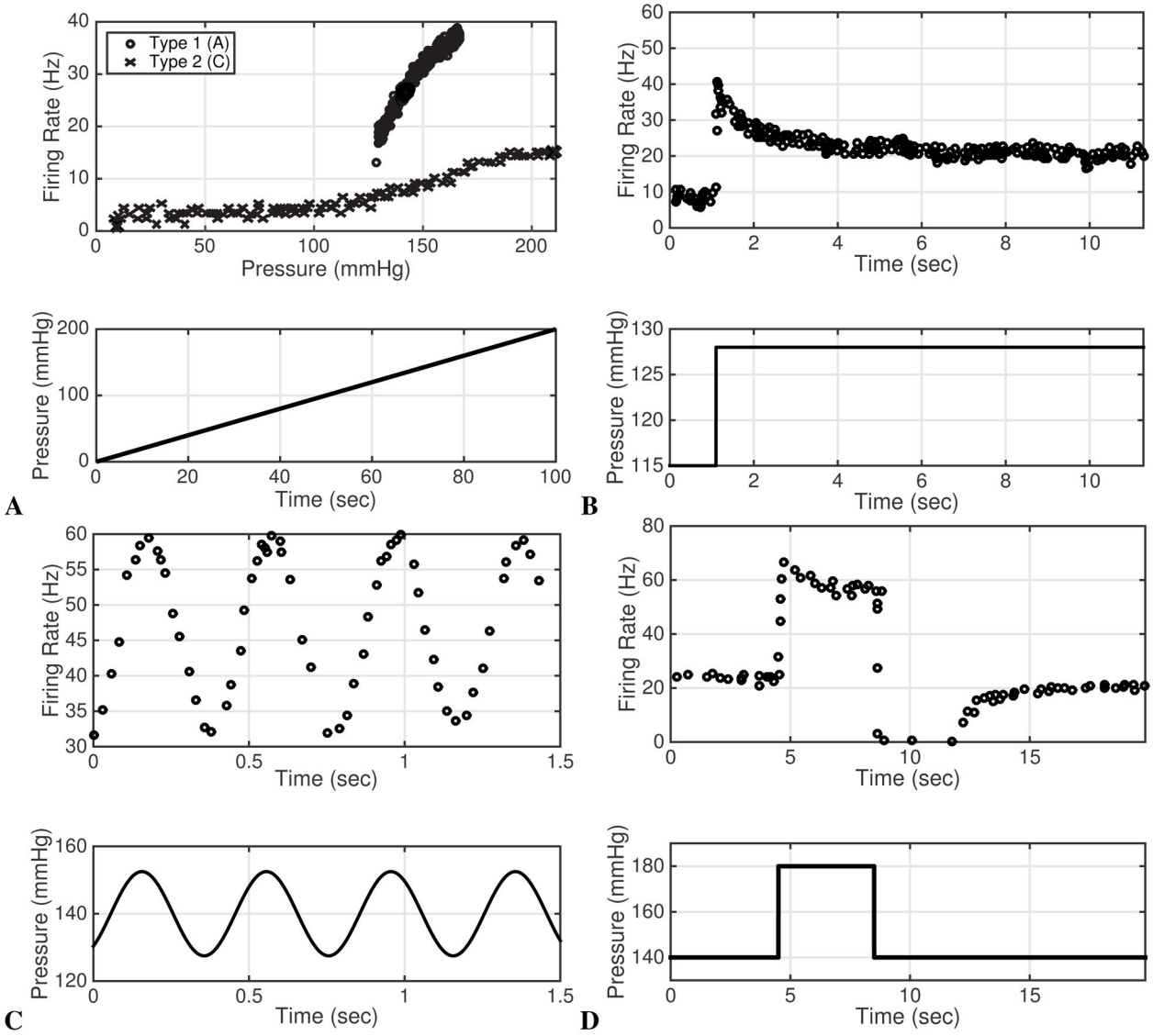

Fig. 3.

A shows a ramp stimulus (bottom) and the associated firing rate response for A- and C-type neurons from a dog carotid artery. Data are extracted from the studies by Schild (1994) and Seagard et al. (1990). **B** shows the step response from a rat A-type neuron (it is believed that some C-type neurons respond in a qualitatively similar manner with a lower firing rate, while others exhibit overshoot, but subsequently ceases to fire), Data extracted from the study by Brown et al. (1978). **C** shows a sinusoidal stimulus and response for a rabbit A-type neuron, data extracted from Franz et al. (1971). C-type firing patterns are reported to be similar but with lower amplitude (See Brown et al. (1978)). **D** shows the pulse pressure stimulus and response for a rat A-type neuron. Note that the neuron cease firing following the pressure drop. Data are extracted from Saum et al. (1976). To our knowledge detailed firing rate recordings of C-type response to a pulse stimulus have been reported.

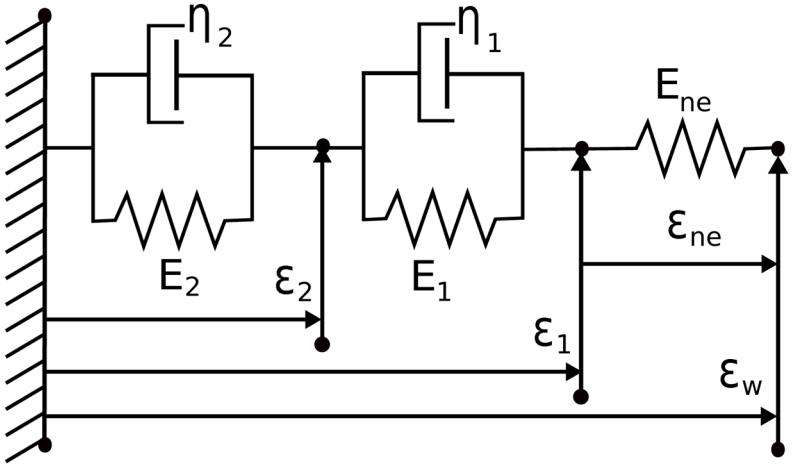

Fig. 4.

Linear mechanical model predicting the transfer of wall strain to the nerve ending strain. The strain across the coupling system is assumed to equal the circumferential wall strain, ε_w. The strain experienced by the spring labeled E_{ne} corresponds to the strain transferred from the wall to the nerve endings, ε_{ne}.

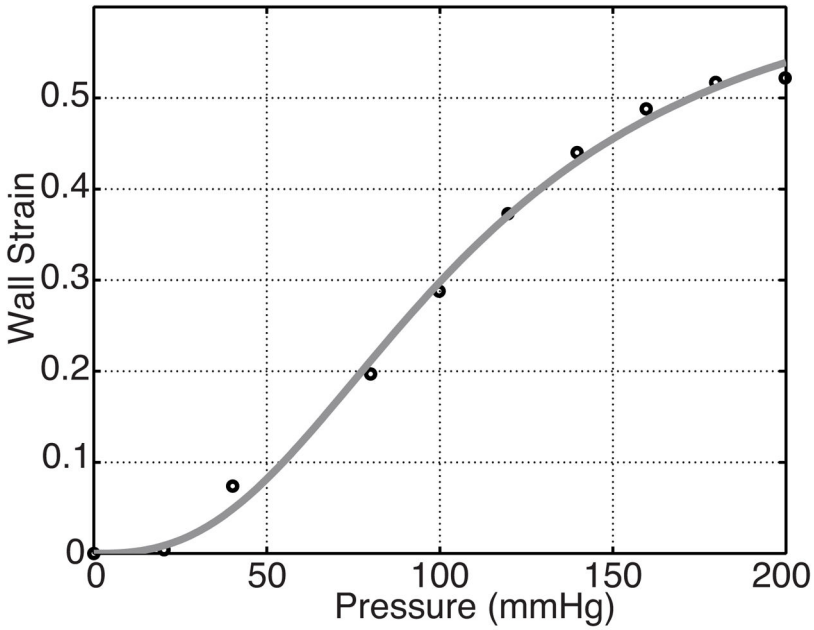

Fig. 5.

Optimized wall strain (6) as a function of pressure along with aortic deformation data from a rat extracted from Feng et al. (2007).

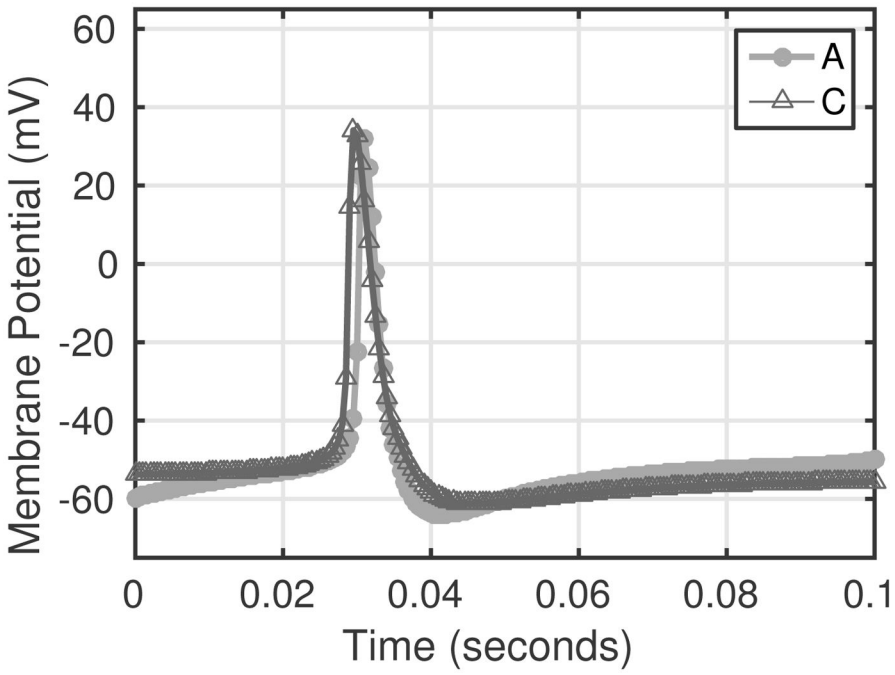

Fig. 6.

Example voltage traces for model simulations using A-type parameters (circles) and C-type parameters (triangles). The A-type action potential is narrower, while the C-type action potential has a slightly wider wave form in agreement with observations reported by Schild et al. (1994).

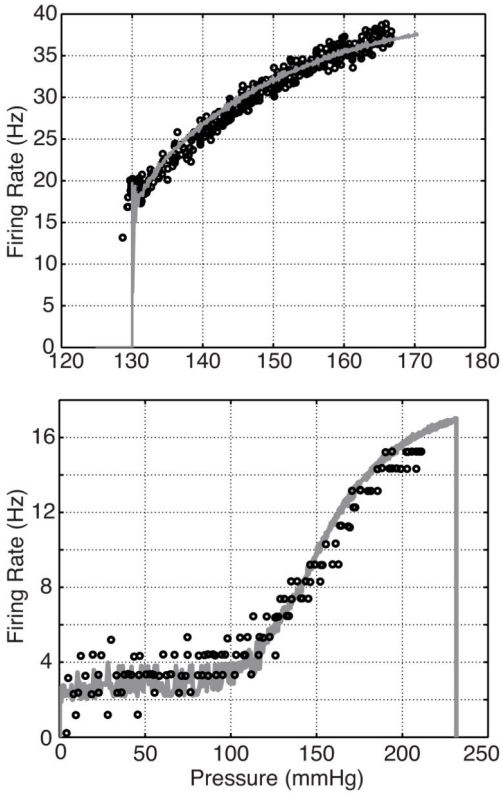

Fig. 7.

Firing rate responses are shown for model simulations with 2 different parameters sets. The parameters used were estimated by minimizing (13) comparing the firing rate output to rat A-type data from ((Schild 1994, Figure 3.4)) (top), whereas those in the bottom panel were estimated against dog C-type data (Note the C-type data are clustered about integer values which is also the case in (Seagard et al. (1990))). We believe this is not physiological, but a result of either the measurement technique or data post-processing used in the study.

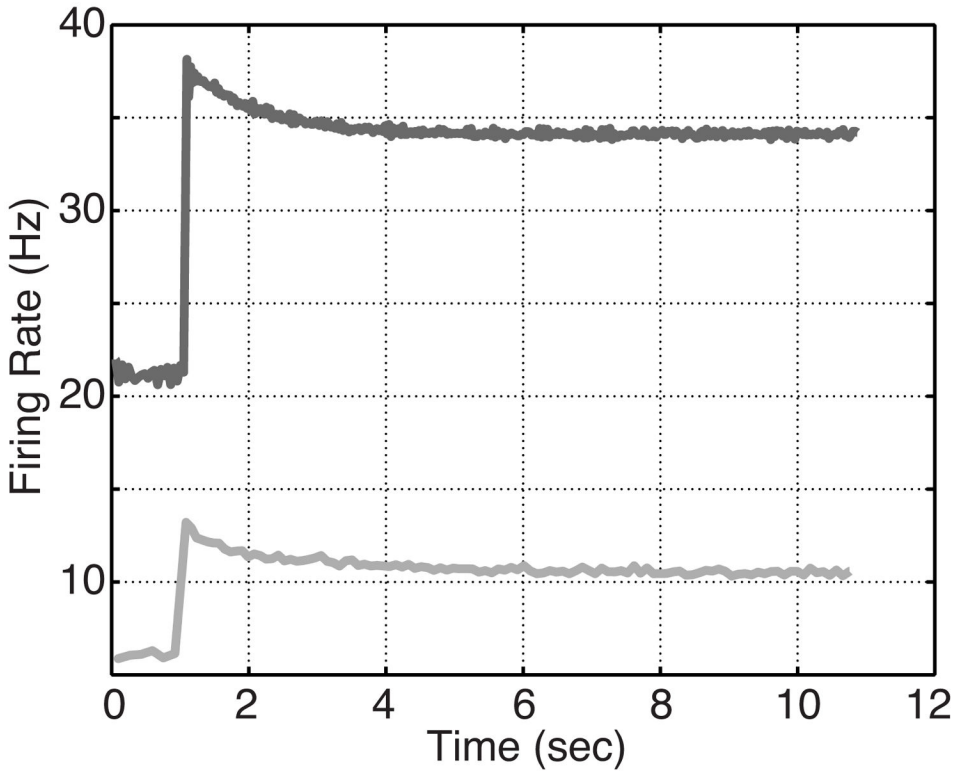

Fig. 8.

Model response to a step pressure input using the model parameters estimated to fit the ramp data: A-type dark, and C-type light.

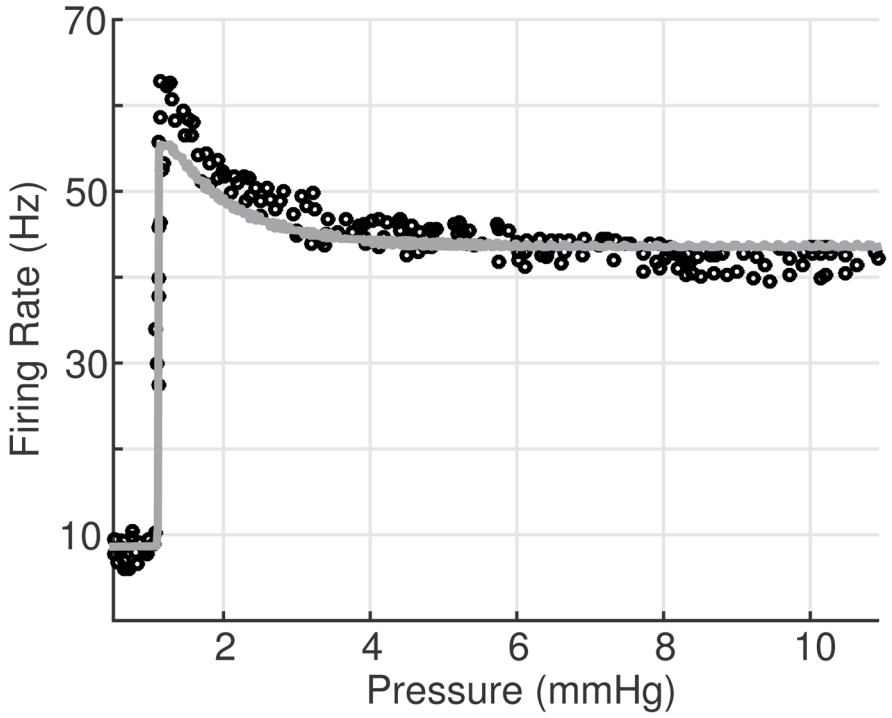

Fig. 9.

Step response for a slowly adapting (rat A-type) neuron observed by Brown et al. (1978), and shown in Fig. 3. Estimated parameter values are reported in Table 1.

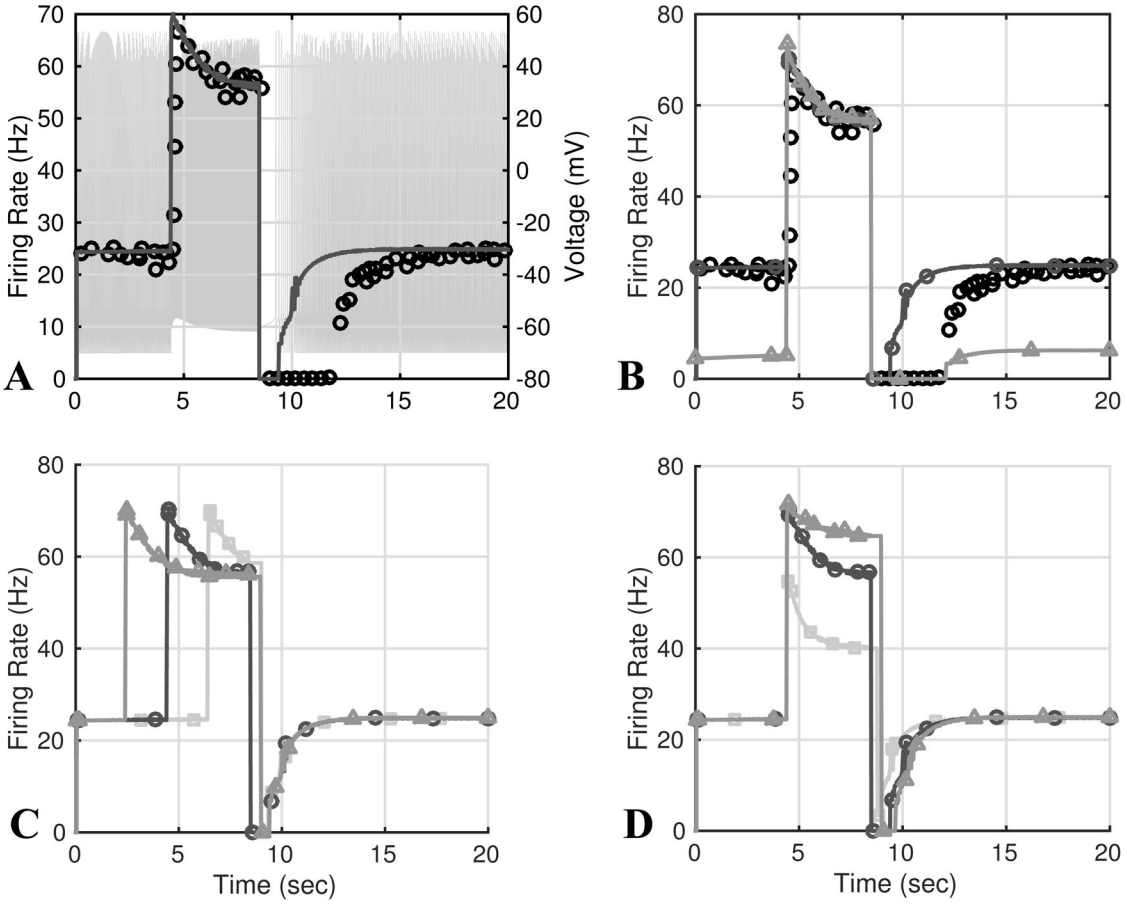

Fig. 10.

Using parameters estimated in response to the step stimulus used in Fig. 9, we were able to reproduce PED. We stimulated the model with a pressure pulse changing from 120 to 156 mmHg with a duration of 4.1 sec and compared the predicted firing rate to that of rat A-type neurons reported by Saum et al. (1976). The computed and experimental firing rates are shown in **A. B** shows results of varying g_m, $\varepsilon_{1/2}$, $S_{1/2}$, and β_2 to match the duration of the PED. These parameter changes results in a lower the baseline firing rate (lighter curve with triangle markers). **C** and **D** show results of increasing the length (2.1 (squares), 4.1 (circles), and 6.1 (triangles) sec) and amplitude (15 (squares), 20 (circles), and 50 (triangles) mmHg) of the pressure pulse.

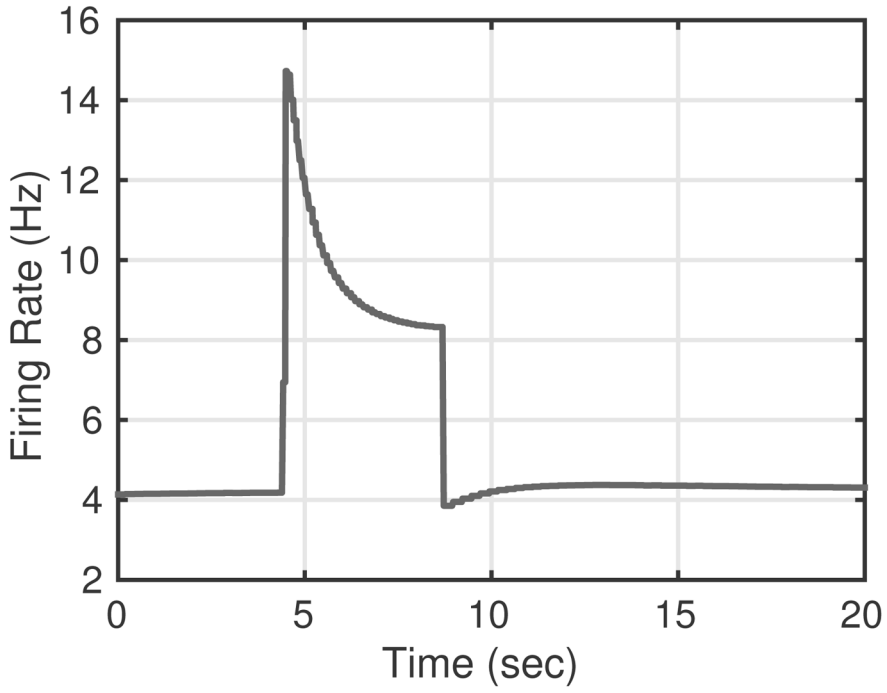

Fig. 11.

Using parameters estimated from fitting the C-type ramp response in Fig. 7, we simulated the C-type neuron's response to a pressure pulse stimulus of the same shape used in Fig. 10. The results show a very peaked overshoot, with a complete lack of PED following the return to baseline pressure.

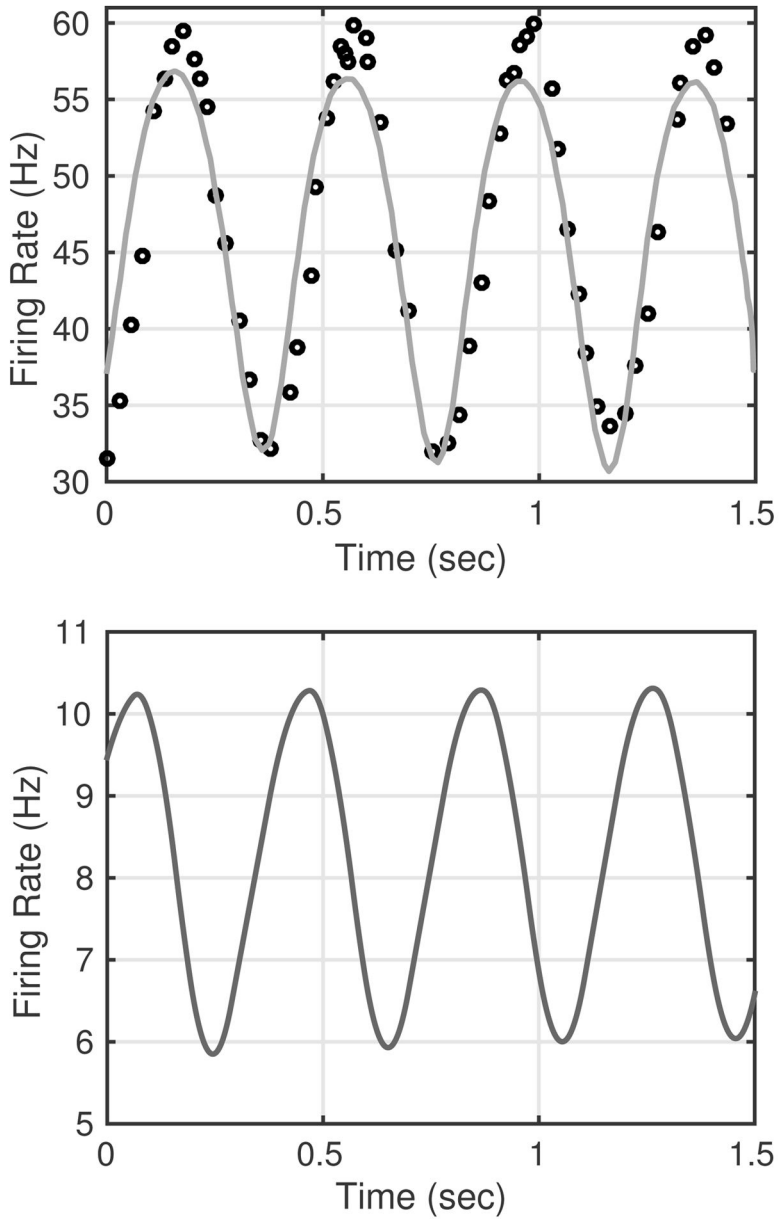

Fig. 12.

Firing rate response to a sinusoidal input (3) with amplitude p_A = 12.5 mmHg, mean p_b = 140 mmHg, frequency ω = 2.5 Hz, and phase shift ϕ = −0.1. The shape of the curve closely fits the experimental data reported by Franz et al. (1971) for A-type rabbit neurons, though the stimulus p_b was adjusted to a higher level than that used to produce the experimental recordings. The resulting estimates of parameters are given in Table 1.

Table 1

Parameters used to fit the various stimuli shown in Fig. 7 and Fig. 9. Neural parameters not estimated are reported in Table 3. The root mean squared error (RMSE) of the model prediction compared to the data is also reported.

Simulation	A-step	A-pulse	A-sine	A-ramp	C-ramp
a_1	5.794×10^{-4}	5.794×10^{-4}	5.804×10^{-4}	1.1550×10^{-4}	1.1712×10^{-4}
a_2	$4.00e\times10^{-4}$	$4.000e\times10^{-4}$	3.976×10^{-4}	3.2473×10^{-4}	5.2057×10^{-4}
β_1	5.2012×10^{-4}	5.2012×10^{-4}	5.255×10^{-4}	3.4971×10^{-4}	2.0641×10^{-4}
β_2	2.00×10^{-3}	2.000×10^{-3}	2.000×10^{-3}	9.8326×10^{-4}	2.500×10^{-3}
$e_{½}$	1.85×10^{-1}	2.10×10^{-1}	1.85×10^{-1}	2.72×10^{-1}	3.048×10^{-1}
$S_{½}$	2.13×10^{-2}	2.13×10^{-2}	2.88×10^{-2}	2.95×10^{-2}	2.46×10^{-2}
$g_{Na,F}$	8.9230	8.9230	10.0197	2.0500	2.0500
$g_{K,dr}$	9.90×10^{-3}	9.90×10^{-3}	9.90×10^{-3}	9.90×10^{-3}	5.50×10^{-3}
$g_{K,A}$	1.68×10^{-1}	1.68×10^{-1}	1.68×10^{-1}	6.30×10^{-2}	3.50×10^{-2}
$g_{K,D}$	1.80×10^{-2}	1.80×10^{-2}	1.80×10^{-2}	1.80×10^{-2}	1.80×10^{-2}
g_m	2.3×10^{-3}	3.0×10^{-3}	2.3×10^{-3}	1.2×10^{-3}	1.0×10^{-4}
C_m	3.25×10^{-2}	3.25×10^{-2}	3.25×10^{-2}	3.25×10^{-2}	3.25×10^{-2}
E_m	0.0	5.0	5.05	0.0	0.0
$g_{Na,B}$	3.25×10^{-4}	4.95×10^{-4}	3.253×10^{-4}	3.25×10^{-4}	3.25×10^{-4}
RMSE	4.611	14.05	2.83	3.565	1.062
R^2	0.8794	0.5793	0.8794	0.6904	0.9394

Table 2

Description of the state variables and auxillary quantities used in this paper.

Variable	Definition	Units
p	aortic blood pressure	mmHg
ε_w	aortic wall strain	unitless
ε_1	nerve ending coupling strain 1	unitless
ε_2	nerve ending coupling strain 2	unitless
ε_{ne}	nerve ending strain	unitless
V	membrane voltage	mV
m	Nav1.7 Activation	unitless
h	Nav1.7 Inactivation	unitless
j	Nav1.7 Reactivation	unitless
n	Delayed Rectifier activation	unitless
p	K A Activation	unitless
q	K A Inactivation	unitless
x	K D Activation	unitless
y	K D Inactivation	unitless
f	firing rate	Hz

Auxillary Quantites	Definition	Units
$I_{Na,F}$	Nav1.7 Current	nA
$I_{K,dr}$	K-DR current	nA
$I_{K,A}$	K-A current	nA
$I_{K,D}$	K-D current	nA
I_m	MSC current	nA
p_o	open probability of MSC	unitless
$I_{Na,B}$	Sodium background leakage	nA
$I_{Ca,B}$	Calcium background leakage	nA
$I_{Na,K}$	Sodium-potassium exchanger current	nA
$I_{Na,Ca}$	Sodium-calcium exchanger current	nA
$I_{Ca,P}$	Sodium-potassium pump current	nA

Table 3

Description of the parameters used in this paper and their nominal values.

Parameter	Definition	Value	Units	Reference
A_0	unstressed aortic area	4.01	mm^2	Valdez-Jasso et al. (2009b)
A_m	maximal aortic area	15.708	mm^2	Valdez-Jasso et al. (2009b)
a	saturation pressure	145	mmHg	Valdez-Jasso et al. (2009b)
κ_w	steepness const	5	unitless	Valdez-Jasso et al. (2009b)
R_A	maximal to minimal area ratio		unitless	
E_0	elastic nerve const	1	mmHg	Bugenhagen et al. (2010)
E_1	elastic nerve const	1	mmHg	Bugenhagen et al. (2010)
E_2	elastic nerve const	5	mmHg	Bugenhagen et al. (2010)
η_1	viscous nerve coupling const	2	mmHg · s	Bugenhagen et al. (2010)
η_2	viscous nerve coupling const	2.5	mmHg · s	Bugenhagen et al. (2010)
α_1	nerve ending const	E_0/η_1	s^{-1}	Mahdi et al. (2012)
α_2	nerve ending const	E_0/η_2	s^{-1}	Mahdi et al. (2012)
β_1	nerve ending relaxation rate	E_1/η_1	s^{-1}	Mahdi et al. (2012)
β_2	nerve ending relaxation rate	E_2/η_2	s^{-1}	Mahdi et al. (2012)
s_1	firing const	480	s^{-1}	Mahdi et al. (2013)
s_2	firing const	100	s^{-1}	Mahdi et al. (2013)
C_m	membrane capacitance	32.5	pF	Schild et al. (1994)
E_{Na}	sodium reversal potential	72.8	mV	Schild et al. (1994)
E_K	Potassium reversal potential	−83.9	mV	Schild et al. (1994)
E_{Ca}	Calcium reversal potential	126.7	mV	Schild et al. (1994)
$g_{Nav1.7}$	maximal Nav1.7 conductance	2.05	μS	Schild et al. (1994)
$g_{K,DR}$	maximal delayed rectifier conductance	0.0055	μS	Schild et al. (1994)
$g_{K,A}$	maximal transient 4AP sensitive conductance	0.035	μS	Schild et al. (1994)
$g_{K,D}$	maximal persistent 4AP sensitive conductance	0.0100	μS	Schild et al. (1994)
$g_{Na,B}$	Background sodium conductance	3.25e-4	μS	Schild et al. (1994)
$g_{Ca,B}$	Background calcium conductance	8.25e-5	μS	Schild et al. (1994)
g_m	mechanosensitive channel conductance	1.00e-4	μS	Alfrey (1997)
$e_{½}$	half activation nerve strain	0.3048	unitless	Alfrey (1997)
$S_{½}$	reciprocal slope for p_o	0.0246	unitless	Alfrey (1997)
$\bar{I}_{Na,K}$	Maximal sodium-potassium exchanger current	0.275	nA	Schild et al. (1994)
$\bar{I}_{Ca,P}$	Maximal calcium pump current	0.0243	nA	Schild et al. (1994)
$[Na^+]_i$	Intracellular sodium concentration	8.90	mM	Schild et al. (1994)
$[Na^+]_o$	Extracellular sodium concentration	154	mM	Schild et al. (1994)
$[K^+]_i$	Intracellular potassium concentration	145	mM	Schild et al. (1994)
$[K^+]_o$	Extracellular potassium concentration	5.40	mM	Schild et al. (1994)
$[Ca^+]_i$	Intracellular calcium concentration	9.70e-05	mM	Schild et al. (1994)

Parameter	Definition	Value	Units	Reference
$[Ca^+]_o$	Extracellular calcium concentration	2.0	mM	Schild et al. (1994)
D_{NaCa}		0.0036	mM^{-4}	Schild et al. (1994)
$K_{M,K}$		0.6210	mM	Schild et al. (1994)
$K_{M,Na}$		5.46	mM	Schild et al. (1994)
$K_{M,CaP}$		0.00005	mM	Schild et al. (1994)
K_{NaCa}		3.6×10^{-5}	$nA \cdot mM^{-4}$	Schild et al. (1994)
γ	exchange ratio	0.5		Schild et al. (1994)
r	exchange ratio	3		Schild et al. (1994)
R	Ideal gas const	8314	J/mol·K	
F	Faraday's const	96500	C/mol	